

# Turbulent structure of air flow over wind-induced gravity waves

Sandro Longo · Miguel A. Losada

Received: 20 November 2011 / Revised: 21 February 2012 / Accepted: 13 March 2012 / Published online: 30 March 2012  
© Springer-Verlag 2012

**Abstract** This is the second paper in a group of three that reports the systematic measurements of wind-generated water waves in a wind tunnel experiment. Here, the structure of the boundary layer on the air side of the water–air interface was analysed and compared with the boundary layer over a smooth plane rigid wall. The contribution of the wave-induced Reynolds stress was detected through filtering the spectrum of velocity fluctuations. Wave-induced Reynolds stresses became negligible for  $z > 5 H_{\text{rms}}$ . The intermittency factor in the boundary layer over water waves was similar to that in a boundary layer over a rigid plane wall, with several differences near the interface. Here, the presence/absence of water damps out the turbulence. The quadrant analyses revealed that ejection and sweep events were dominant and more concentrated. At small fetches, the large-amplitude negative streamwise perturbations were preferentially lifted. Turbulence energy production peaked at  $z/\delta = 0.2$  and had a distribution similar to that observed for a self-preserving boundary layer with a strong adverse gradient pressure. The quadrant analysis contribution to the energy production revealed that ejections still dominated the balance and that the production was spatially modulated in the wind direction with a couple of cells and with a minimum in the area of the free surface wave height reduction.

## Abbreviations

|                                   |  |
|-----------------------------------|--|
| $\overline{\quad}$                | Time average operator  |
| $\widetilde{\quad}$               | Oscillating term operator                                      |
| $\overline{\quad}$                | Phasic average operator  |
| $\Phi$                            | Volume fraction or concentration for water                     |
| $\delta$                          | Boundary layer thickness                                       |
| $\gamma$                          | Intermittency factor   |
| $\rho$                            | Mass density   |
| $\theta$                          | Angle between wind and wave propagation direction              |
| $\kappa$                          | Turbulent kinetic energy                                       |
| $\nu$                             | Kinematic fluid viscosity                                      |
| $a$                               | Exponent   |
| $a_c$                             | Crest height   |
| $a_t$                             | Trough height  |
| $C$                               | Concentration  |
| $c$                               | Celerity of propagation of the gravity waves                   |
| $d$                               | Water depth  |
| $H$                               | Wave height, threshold coefficient                             |
| $H_{\text{rms}}, H_{\text{mean}}$ | Root mean square wave height, mean wave height                 |
| $H_{1/3}$                         | Highest one-third wave   |
| $k$                               | Coefficient, von Karman constant                               |
| $L$                               | Wave length  |
| p.d.f.                            | Probability distribution function                              |
| Re, $Re_x$                        | Reynolds number, based on the abscissa $x$                     |
| $t$                               | Time   |
| $T_{\text{mean}}, T_{1/3}, \dots$ | Period of the waves, mean value, mean value of the first third |
| TKE                               | Turbulent kinetic energy                                       |
| $U$                               | Streamwise wind velocity                                       |
| $U_\infty$                        | Asymptotic wind velocity                                       |

S. Longo (✉)  
Department of Civil Engineering, University of Parma,  
Parco Area delle Scienze, 181/A, 43100 Parma, Italy  
e-mail: sandro.longo@unipr.it

M. A. Losada  
Centro Andaluz de Medio Ambiente, Universidad de Granada,  
Avda. del Mediterraneo s/n, 18006 Granada, Spain

|                |  |
|----------------|--|
| $U_{10}$       | Wind velocity at the reference level of 10 m   |
| $U_s$          | Drift velocity                                 |
| $U, V$         | Streamwise, vertical wind velocity             |
| $U', V'$       | Streamwise, vertical fluctuating wind velocity |
| $u_*$          | Friction velocity in the air boundary layer    |
| $x, y, z, x_i$ | Spatial co-ordinates                           |
| $z_s$          | Instantaneous level of the free surface        |

## 1 Introduction

The interaction between the atmospheric boundary layer and water waves is considered the most important mechanism to explain the momentum transfer from wind to water. Both the inviscid Miles model (Miles 1957) and the viscous Miles model (Miles 1959) underpredict the wave growth rate. The importance of the feedback mechanism, with the wave-induced Reynolds stresses having the same order of magnitude as other disturbances in the air stream, requires insight into the structure of the air-flow boundary layer. The analysis can be performed by either separating the wave-induced contribution to the turbulence, i.e., phase-resolving the experimental data, or considering the turbulence effects as an average between the self-turbulence and wave-induced turbulence. Phase-resolving the experimental data requires sufficiently regular periodic water waves, for at least the dominant wave; otherwise, non-linear interactions of the velocity fluctuations induced by different waves greatly complicate the scenario. The air boundary layer and the free surface elevations must be measured simultaneously. These conditions can easily be met if the wind is blowing over mechanically generated regular waves, as in Stewart (1970) and Hsu and Hsu (1983), but are difficult to satisfy if the waves are directly generated by wind, unless an equivalent dominant wave is defined. The spectrum of the elevation of the water waves in the generation area is broad, with several strongly interacting components, which peak to a limited range of frequencies in the area where the non-linear, wave-wave interaction favours the collapsing of the different wave components.

A wide review of the experiments on wave-induced motion in the wind stream is reported in Shaikh and Siddiqui (2011a, b), who used particle image velocimetry (PIV) to resolve in phase velocity, vorticity and Reynolds stress in the airside field over wind-generated waves. A still debated problem is about the transfer mechanism details of momentum at the interface. Some authors (Kato and Sano 1971; Antonia and Chambers 1980) report that young short gravity waves extract momentum from the wind, while developed waves transfer momentum to the wind. The

recent paper by Shaikh and Siddiqui (2011a) reports that young short gravity waves also transfer momentum to the air, with a two-way transfer differentiated in magnitude and sign according to the wave phase.

In order to go in deeper details of the transfer phenomena in the boundary layer, other different tools can be used. Quadrant analysis is a commonly used tool to quantify the mechanisms of the exchange in the boundary layer; it is a conditional averaging method in which the flow is classified according to the quadrant in which the two velocity components fluctuations fall (ejection, sweep, outward and inward interactions) and that can be used to explore the Reynolds shear stresses contribution to the momentum and energy balance. This analysis has been widely used to reveal the turbulent structure in the wall boundary layer over a rigid wall (Alfredsson and Johansson 1984) and to find the most significant form of disturbance (Nolan et al. 2010). Also, Foster et al. (2006) analysed the near-surface coherent structures in a large-eddy simulation of the marine boundary layer using the quadrant analysis, finding the dominance of the upward ejections of the slower moving near-surface air and of the downward sweeps of higher speed air from higher in the boundary layer.

Sullivan et al. (2008) found that in the quadrant analysis of the momentum flux a wave age dependence is predicted (the wave age is the ratio between the wave phase celerity and the wind asymptotic velocity acting along the wave propagation direction), and the measured bulk drag coefficient depends on wind speed and wave state (e.g., a light wind-following swell gives a drag coefficient approximately 50 % lower than a standard evaluation without including the sea state dependency).

The surface drag is a widely used parameter to evaluate the efficiency in momentum transfer. This topic was treated in Longo (2012) in the present context of experiments and there are several works dealing with the drag in deep water waves, but less detailed studies on the surface drag in the surf-zone and, in general, in shallow water. According to Letchford and Zachry 2009, although yet to be determined, the surface drag coefficient in shallow water is hypothesised to be significantly larger than in deep water due to: (1) decrease in the wave phase speed, (2) increase in wave height and steepness in the shoaling region and at the onset of wave breaking, (3) rapidly varying surface wave field, (4) waves may not align with the mean wind near the shore, and (5) broken waves can cause an increase in the local sea surface roughness past the initial breaking region.

Quadrant analysis and the boundary layer structure are inherently connected to intermittence. Intermittence is present at all length scales and describes the fluid velocity as a composition of a mean value; a time varying but almost deterministic component and a purely random component. The second contribution is attributed to coherent structures.

Coherent structures transport the purely random contribution by convection that results in the flow field being partially or completely filled with turbulence. The consequence of the active presence of coherent structures, and hence of intermittency, is that the phenomenological turbulence model should not only be based on the characteristics of the mean flow but also include the advection effects of the vortices at different length and time scales.

The interest in turbulence analysis in the presence of waves is also due to the experimental evidence that a single parameter chosen to describe the interface geometry, e.g., the root mean square wave height, is inadequate to describe the characteristics of the wave boundary layer, because walls with identical roughness values can generate different turbulence. This conclusion holds true for fixed walls (Krostad and Antonia 1999) and should be even more evident for mobile and interacting ‘walls’. Conceptually relevant is the recent contribution by Hunt et al. (2011) on the interactions between shear-free turbulence on either side of a nearly flat horizontal interface, focussed on gas–liquid interfaces on where turbulence is generated either above or below the interface, even though the hypothesis of nearly flat interface is clearly met only at the early stage of waves generation. More relevant to the present context is the contribution by Donelan et al. (2006), focussed on the momentum transfer from wind to waves through wave-induced pressure acting on the slopes of the waves, i.e., the so-called form drag. Donelan et al. (2006) report on measurements obtained in a lake, an environment where the wave celerity is limited by the shallow water, hence the waves are correspondingly steep. For very strong forcing a full separation of the air flow field occurs at the wave crest, with a consequent reduction in the efficiency of momentum transfer. This regime is classified as ‘skimming regime’ in Letchford and Zachry (2009). This is confirmed by a numerical simulation of turbulent flow over idealised water waves (not evolving under the action of the wind) by Sullivan et al. (2000) that show that the imposed waves significantly influence the mean flow, vertical momentum fluxes, velocity variances, pressure, and form drag. With increasing wave age, the surface roughness decreases so that the wavy lower surface is nearly as smooth as a flat lower boundary. Vertical profiles of turbulence statistics show that the wave effects depend on wave age and wave slope but are confined to a region  $kz < 1$  (where  $k$  is the wavenumber of the surface undulation and  $z$  is the vertical coordinate). The turbulent momentum flux can be altered by as much as 40 % by the waves.

In general, there are several specific mechanisms that control the transfer phenomena at the interface, and to clarify them helps the understanding of the whole process. A better description of the air–water boundary conditions is also important in order to improve the accuracy of

numerical models (see, e.g., Brocchini and Peregrine 2001 and Brocchini 2002).

Notably, turbulence dynamics is essentially a 3D phenomenon (e.g., vortex stretching and the energy cascade mechanisms require three dimensionality), hence 2D experiments do not guarantee an holistic approach to the analysis. However, it is a common limitation for most of the previous experimental investigations (Rashidi and Banerjee 1990; Lam and Banerjee 1992). Due to the restriction of the laboratory conditions, a three-dimensional investigation has not been possible but care has been taken in interpolating the results, and all the instruments used have been validated against other independent experiments and analytical solutions. The details of the experimental setup, including the free surface statistics and the mean properties of the air-side boundary layer, have been described in Chiapponi et al. (2011) and analysed in detail in Longo (2012). Further aspects on the water side flow field are given in Longo et al. (2012).

This paper is organised as follows: Sect. 2 describes the experimental apparatus. In Sect. 3, the Reynolds stresses and the turbulence structure in the air boundary layer are detailed, and intermittency is analysed in Sect. 4. In Sect. 5, the quadrant analysis is reported, and in Sect. 6, turbulence production is addressed. The conclusions are presented in the last section.

## 2 Experimental apparatus and mean parameters

The experiments were conducted in a small non-closed low-speed wind tunnel in the Centro Andaluz de Medio Ambiente, CEAMA, University of Granada, Spain. The boundary layer wind tunnel has a poly(methyl methacrylate) (PMMA) structure with a test section of 3.00 m in length with a 360 mm × 430 mm cross-section. The wind velocity, up to 20 m/s, is controlled by a variable frequency converter controlling an electric fan in the downstream section with a maximum power of 2.2 kW. The air flow is straightened by a honeycomb section connected to the tunnel followed by a contraction. A water tank is installed to allow water wave generation. The water tank is constructed of PVC and is 970 mm long and 395 mm high (internal size), while the still water depth is 105 mm. The overall layout is shown in Fig. 1. The air flow cross-section over the tank is 235 mm × 430 mm and is connected to the wind tunnel through an upstream ramp and a downstream ramp. The upstream ramp avoids air flow separation and guarantees a stable thin boundary layer above the water surface. The downstream ramp is required to reduce energy loss and avoid large unsteady vortices, which can induce pulsating motions in the air stream, hence smooth air flow can be maintained. At the downstream end of the tank, the

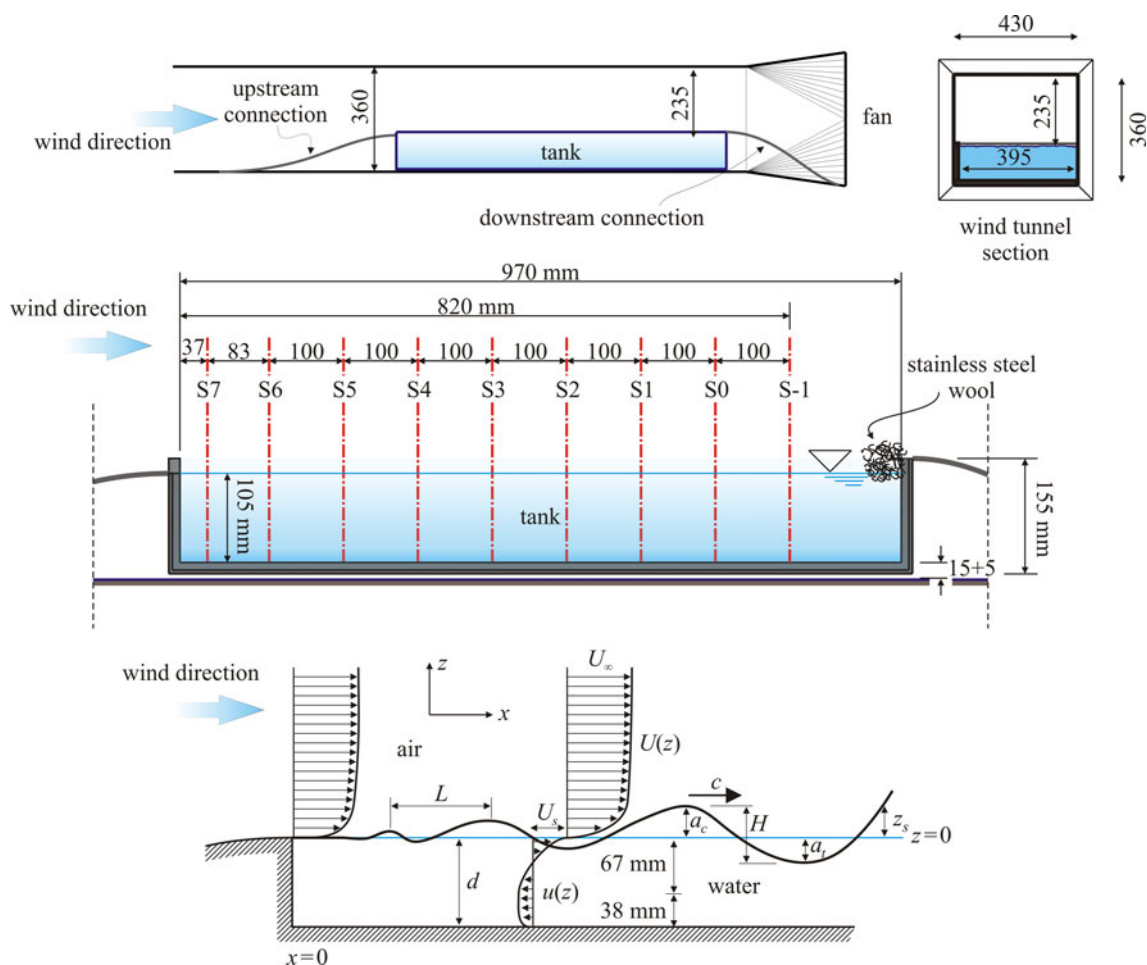


**Fig. 1** Layout of the wind tunnel and the water tank

PVC side is slightly higher than the upstream side wall to limit the overtopping of generated waves, and a wave absorbing system of stainless steel wool is used to minimise reflection.

One side of the tank is constructed of glass (thickness 5 mm) to allow optical access. The details of the flow field and definition of symbols are also shown in Fig. 1. Further details can be found in Chiapponi et al. 2011.

## 2.1 Fluid velocity measurements

The wind speed in the tunnel is measured with a TSI 2D Laser Doppler velocimetry (LDV) system.

The laser source is an Innova 70 Series water-cooled Ar-Ion laser, which can reach a maximum power of 5 W and works with two pairs of laser beams with different wavelengths (green,  $\lambda_g = 514.5$  nm and blue,  $\lambda_b = 488.0$  nm); each pair define a plane, and the two planes are perpendicular to each other. The TSI optical modular system has a two-component fibre optics transmitting/receiving probe,

which also collects the scattered light, sending it to the elaboration system, as the system works in backward scatter mode. The focus length of the probe lens is 363 mm, and the beam spacing is 50 mm. The half-angle between the incident beams is  $3.96^\circ$ . The measurement volume is defined by the intersection of the four laser beams, and has the shape of a prolate ellipsoid whose dimensions are  $\sim 0.08$  mm  $\times$  0.08 mm  $\times$  1.25 mm.

The transmitting/receiving equipment of the LDV is mounted on an ISEL traverse system and is placed adjacent to the wind tunnel. The traverse system allows longitudinal (parallel to the wind tunnel) and vertical displacements of the probe, which are controlled by a MATLAB<sup>®</sup> programme that transfers data to a Controller ISEL C142 4.1. The stepper motors of the traverse system have a resolution of 1 step = 0.0125 mm, but the overall accuracy in the probe position is expected to be equal to 0.1 mm.

The reference system for the transverse displacements and the velocity measurements has its horizontal origin ( $x = 0$ ) at the upstream end of the water tank and its

vertical origin ( $z = 0$ ) at the still water level. The position of the still water level was defined at the beginning of each series of measurements, moving the probe in the vertical in order to have the intersection of the LDV beams exactly at the free surface. The signal of a correct vertical positioning was a huge increment of data rate, due to the particles of dust in random motion at the interface.

The last parameter set for the LDV velocity measurements is the orientation of the laser beams. The laser coordinate system can be rotated by an angle  $\theta$  with respect to the external coordinate system made of the horizontal ( $x$ ) and vertical ( $z$ ) axes. For the present experiments, a rotation  $\theta = 45^\circ$  is set to reach points close to the interface.

For measurements in the air, water drops generated by a spray gun are used for seeding. The spray gun is outside of the wind tunnel, with the nozzle pointed towards the honeycomb section at the entrance of the wind tunnel. This setup ensures that the large water droplets are captured by the honeycomb section and that only the fine droplets reach the test section. The strong effects that surfactants have on water wave generation necessitate the regular cleaning of the wind tunnel and the water tank. The LDV system measures the velocity of the particles and not of the fluid; however, small light particles follow the fluid motion well, as indicated by many studies.

The uncertainties in the LDV systems arise from velocity bias, the inhomogeneous distribution of tracer particles, errors in the individual velocity measurements, velocity gradients in the measurement volume, errors in the optical system, low resolution of the detector and the signal processing. These sources may be viewed as different types of noise that represent the white noise from stray light (reflections or scattering of laser light from walls, windows or optical components), the photomultiplier and the associated electronics. A weighting function based on the transit time was applied to correct the velocity bias due to the dependence of the sampling on the velocity magnitude. The overall uncertainty is equal to  $\sim 1\%$  of the estimated velocity. The measurements last for 600 s except for some tests with data overflow, which limits the time of acquisition to no less than 400 s.

During the tests, the mean water level is reduced due to evaporation and overtopping of the generated waves. To control the mean water level, the tank is connected to a piezometer through a plastic tube to avoid the water level fluctuations. An ultrasound distance metre measures the water level in a piezometer connected to the water tank. The operator periodically reads the water level in the piezometer as detected by the ultrasound distance metre and fills up the wave tank through the tube if the variation is greater than 0.2 mm. The accuracy of the mean water level position is expected to be within 0.3 mm.

After turning on the wind tunnel fan, it is necessary to wait long enough for the air stream and for the water level control system to reach a stationary state. In fact, immediately after the start of the fan, a pressure reduction on the free surface of the wave tank is responsible for a reduction of the water level in the piezometer. This variation is always less than 10 mm, equivalent to  $\sim 1$  mbar, and accordingly, a tiny mass flux from the piezometer tank towards the wave tank is generated. The effect is simply due to the pressure gradient (with respect to the atmospheric pressure) generated by the initiation of the fan.

To check the characteristics of the external flow field and validate the wind tunnel in the modified configuration (with the contraction/expansion elements upstream and downstream of the water tank), the first series of experiments were conducted with the air flow over a plain, smooth PVC wall, rather than the air–water interface.

## 2.2 The water level measurements

The water level can be measured using three different instruments: an ultrasound distance metre in the air, positioned on top of the wind tunnel; resistance probes in the sections of the measurements; and the echo output of the ultrasound Doppler velocity profiler. For the free surface data analysis the resistance probes are preferred. There are 8 resistance probes always connected and positioned in sections from S7 to S0. Occasionally, an additional resistance probe in Section S-1 (the largest fetch) is connected but most of the results of the water level measurements in Section S-1 have been obtained with the ultrasound Doppler velocity profiler. The resistance probes are quite accurate but have a limitation in resolution in the order of the height of the water meniscus around the wires. Also, the cross-talking influences the measurements, and even though the probes are positioned with the two wires aligned along the expected wave crest (i.e., spanwise), the spatial resolution can be assumed to be equal to the spacing of the wires. The probes have the advantage of simultaneous measurement in several sections and hence the possibility of cross-correlation of the water level elevations used to evaluate the phase and the group celerity of the gravity waves (see Longo 2012).

The water level measurements are performed simultaneously at all sections (S0 to S7) using the 8 resistance probes, and the data are acquired at a rate of 200 Hz through a DAQ board after filtering with a low-pass filter at 20 Hz. The hardware is produced by DHI (water level modules, filter, DAQ), but the 8-wave gauges were produced in the lab with twin parallel wires ( $\phi = 0.3$  mm) at a spacing of 20 mm. The calibration is conducted by modifying the water level in the expected range and measuring the input value through an ultrasound distance metre

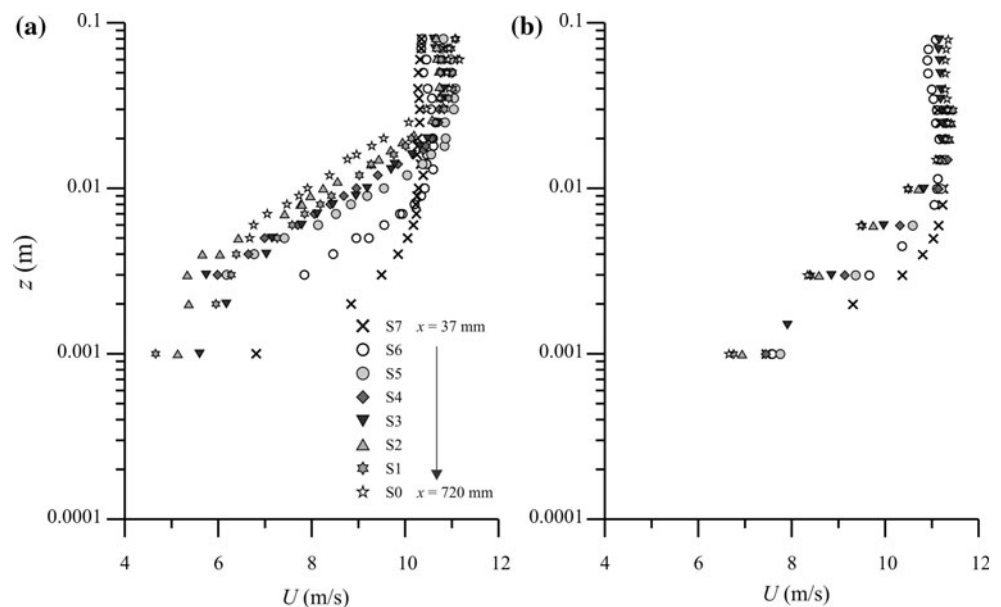
**Table 1** Statistics of the waves generated by the maximum wind speed test ( $U_\infty = 10.90$  m/s): wave height, crest and trough amplitude

| Section # | $x$ (mm) | $H_{\text{rms}}$ (mm) | $a_{\text{c-rms}}$ (mm) | $a_{\text{t-rms}}$ (mm) | $H_{\text{ave}}$ (mm) | $H_{1/3}$ (mm) | $H_{1/10}$ (mm) | $H_{1/20}$ (mm) | $H_{\text{max}}$ (mm) |
|-----------|----------|-----------------------|-------------------------|-------------------------|-----------------------|----------------|-----------------|-----------------|-----------------------|
| S7        | 37       | 2.00                  | 1.31                    | 1.13                    | 1.66                  | 2.97           | 4.04            | 4.51            | 7.63                  |
| S6        | 120      | 3.93                  | 2.26                    | 2.11                    | 3.28                  | 5.82           | 7.81            | 8.67            | 13.21                 |
| S5        | 220      | 6.02                  | 3.44                    | 3.06                    | 4.97                  | 9.01           | 11.89           | 13.07           | 18.41                 |
| S4        | 320      | 6.20                  | 3.56                    | 3.21                    | 5.06                  | 9.27           | 12.46           | 13.83           | 19.22                 |
| S3        | 420      | 5.73                  | 3.30                    | 2.99                    | 4.77                  | 8.49           | 11.32           | 12.53           | 17.84                 |
| S2        | 520      | 5.46                  | 3.17                    | 2.90                    | 4.52                  | 8.10           | 10.93           | 12.20           | 18.18                 |
| S1        | 620      | 5.41                  | 3.18                    | 2.89                    | 4.44                  | 8.01           | 11.08           | 12.49           | 17.60                 |
| S0        | 720      | 5.64                  | 3.29                    | 3.00                    | 4.62                  | 8.40           | 11.52           | 12.83           | 19.65                 |

$H_{1/3}$  is the average height of the top 1/3 wave heights (the waves in the record are counted and selected in descending order of wave height, from the highest wave until 1/3 of the total number of waves was reached. The mean of their heights is  $H_{1/3}$ )

**Fig. 2** The horizontal mean wind velocity profiles.

**a** Measurements in air over water,  $U_\infty = 10.90$  m/s;  
**b** measurements in air over a plane smooth rigid wall,  $U_\infty = 11.30$  m/s



installed in the wind tunnel over the tank. The hardware modules are set with the maximum gain and with the zero offset corresponding to an empty tank.

The computed surface wave statistics are summarised in Table 1 (from Longo 2012).

### 2.3 The results for the mean flows

To analyse the air-flow boundary layer, the fan speed was set at a specific value resulting in a wind velocity  $U_\infty = 10.90$  m/s, and the air velocity was measured at several points in sections S0–S7, with a spacing of 1 mm near the interface and a larger spacing in the upper region. The mean horizontal velocity profiles are shown in Fig. 2a in dimensional variables. Similar velocity profiles were observed for flow over a smooth plane horizontal wall (Fig. 2b). The velocity exhibited a logarithmic profile, where the coefficients were evaluated by a curve fitting

procedure. Table 2 presents the measurements over the waves, and Table 3 presents the measurements over the plane smooth wall. The details are reported in Longo (2012).

### 3 Reynolds stresses and turbulence

The instantaneous velocity typically comprises mean and turbulent components, but in the presence of water waves, a wave-induced component is also present. Therefore, the generic variable can be written as:

$$U(x, z, t) = \overline{U}(x, z) + \tilde{U}(x, z, t) + U'(x, z, t), \quad (1)$$

where  $U(x, z, t)$  is the instantaneous velocity, the variable with an overbar is the (time) mean velocity, the variable with a tilde is the wave-induced (oscillating) component, and the variable with the prime is the fluctuation

**Table 2** Parameters for the mean velocity profiles at different fetches

| Section #            | S7    | S6    | S5    | S4    | S3    | S2    | S1    | S0    |
|----------------------|-------|-------|-------|-------|-------|-------|-------|-------|
| $x$ (mm)             | 37    | 120   | 220   | 320   | 420   | 520   | 620   | 720   |
| $U_\infty$ (m/s)     | 10.30 | 10.50 | 10.93 | 10.72 | 10.74 | 10.72 | 10.94 | 10.92 |
| $u_*$ (m/s)          | 0.39  | 0.40  | 0.74  | 0.71  | 0.68  | 0.72  | 0.63  | 0.63  |
| $\delta$ (mm)        | 3.9   | 9.4   | 18.0  | 19.1  | 21.2  | 24.6  | 28.0  | 36.2  |
| $Re_x (\times 10^5)$ | 0.252 | 0.834 | 1.59  | 2.27  | 2.99  | 3.69  | 4.49  | 5.21  |

Measurements in air over water.  $U_\infty$  is the asymptotic velocity,  $u_*$  is the friction velocity,  $\delta$  is the boundary layer thickness, and  $Re_x$  is the Reynolds number based on the fetch extension

**Table 3** Parameters for the mean velocity profiles at different fetches

| Section #            | S7    | S6    | S5    | S4    | S3    | S2    | S1    | S0    |
|----------------------|-------|-------|-------|-------|-------|-------|-------|-------|
| $x$ (mm)             | 37    | 120   | 220   | 320   | 420   | 520   | 620   | 720   |
| $U_\infty$ (m/s)     | 11.30 | 11.30 | 11.30 | 11.30 | 11.30 | 11.30 | 11.30 | 11.30 |
| $u_*$ (m/s)          | 0.35  | 0.35  | 0.39  | 0.43  | 0.44  | 0.52  | 0.54  | 0.53  |
| $\delta$ (mm)        | 4.2   | 7.2   | 12.7  | 13.0  | 13.8  | 14.4  | 15.6  | 15.7  |
| $Re_x (\times 10^5)$ | 0.277 | 0.898 | 1.65  | 2.39  | 3.14  | 3.89  | 4.64  | 5.39  |

Measurements in the air over a plane smooth solid wall. For symbols, see Table 2

component. The wave-induced velocity becomes important in the momentum transfer across the interface, even though its effect is not monotonic; for increasing forcing, the separation of the wind flows occurs at the wave crest and the wave-induced pressure perturbation increases, but for very strong forcing this pressure perturbation is much reduced and a sort of skimming flow is retained with a limited drag coefficient (see Donelan et al. 2006). The evaluation of the wave-induced velocity requires the instantaneous interface position measurements to perform a phase average (Hsu et al. 1981), which is not the case here. Hence, most of the data analysis in the present work is based on decomposing the instantaneous velocity into a mean (time average) component and a fluctuating component, which includes the wave-induced contribution:

$$U(x, z, t) = \bar{U}(x, z) + U'(x, z, t), \tag{2}$$

and only for an estimation of the effects of the wave-induced velocity in Section *Estimation of the effects of the gravity waves on turbulence within the air boundary layer*, the decomposition in Eq. (1) is adopted.

In the following section, the Reynolds stress tensor is analysed and compared with that measured over a plane smooth rigid wall.

### 3.1 The Reynolds stress tensor

The turbulent kinetic energy (TKE) and the Reynolds shear stress over water and the plane smooth rigid wall are shown in Figs. 3 and 4. The asymptotic wind speed was essentially the same in the two tests (it was slightly reduced in

the presence of water waves due to the additional resistances; the fan power was the same), but the kinetic energy level and the Reynolds shear stress level were strongly enhanced in the presence of waves by up to three times.

A close-up of the components of the Reynolds tensor components near the interface in Section S2 is shown in Figs. 5 and 6. In the presence of water waves, the stress distribution is similar to that measured over a flat plate (Schlichting and Gersten 2000; Hsu et al. 1981). A layer of constant shear stress  $-\overline{U'V'}$  was observed. Assuming that this stress also acts at the upper boundary of the viscous sub-layer, the result of the air flow over water waves is the following:

$$-\frac{\overline{U'V'}}{U_\infty^2} = \left(\frac{u_*}{U_\infty}\right)^2 \simeq 0.0065 \rightarrow u_* = 0.86 \text{ m/s}. \tag{3}$$

This value is 19 % larger than the friction velocity computed by fitting the mean horizontal velocity profile, which gives 0.72 m/s (Table 2). The difference can be attributed to the possible reduction of the stress near the water interface (see Fig. 9 in Longo 2011), considering that the closest useful point of the measurements was at  $z^+ = 100$ , i.e., in the inertial sub-layer. The possible reduction can be addressed to the swapping of the role between Reynolds stresses and viscous stresses in the subsurface layer, dominated by the viscosity.

The result of the air flow over the plane smooth solid wall is the following:

$$-\frac{\overline{U'V'}}{U_\infty^2} = \left(\frac{u_*}{U_\infty}\right)^2 \simeq 0.0025 \rightarrow u_* = 0.56 \text{ m/s} \tag{4}$$

**Fig. 3** Turbulent kinetic energy. **a** Measurements in air over water,  $U_\infty = 10.90$  m/s; **b** measurements in air over a plane smooth rigid wall,  $U_\infty = 11.30$  m/s

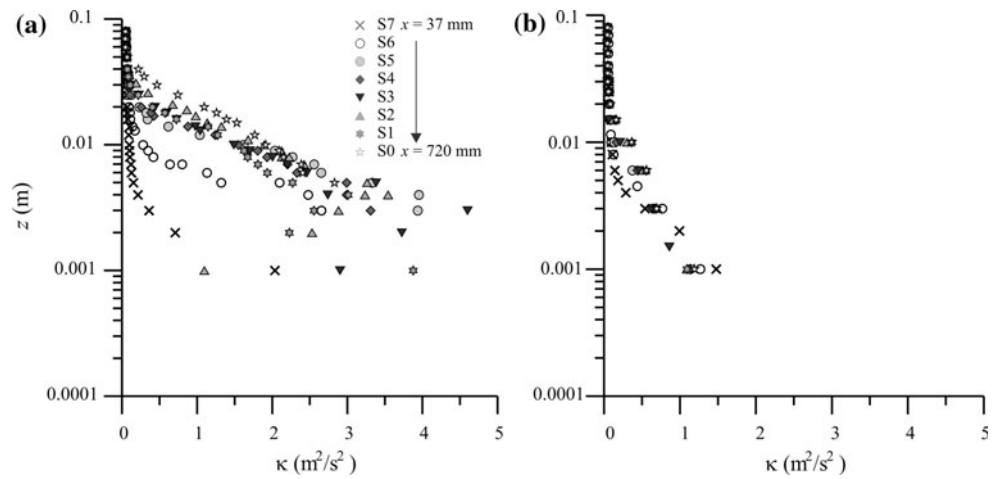


**Fig. 4** Reynolds shear stress. **a** Measurements in air over water,  $U_\infty = 10.90$  m/s; **b** measurements in air over a plane smooth rigid wall,  $U_\infty = 11.30$  m/s

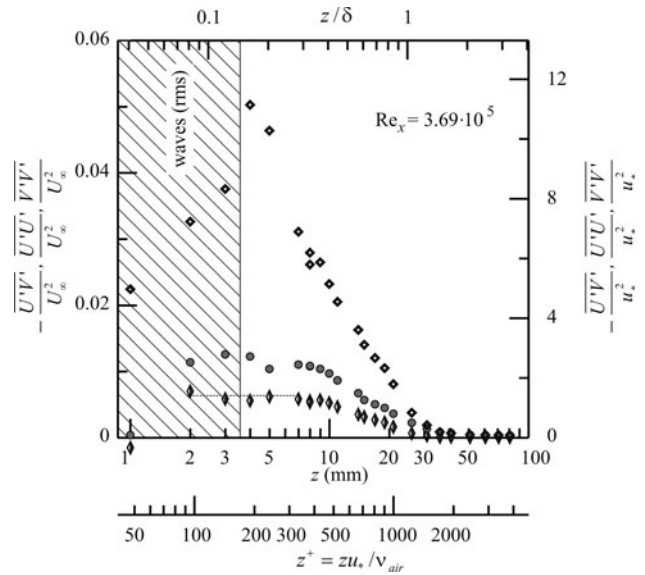
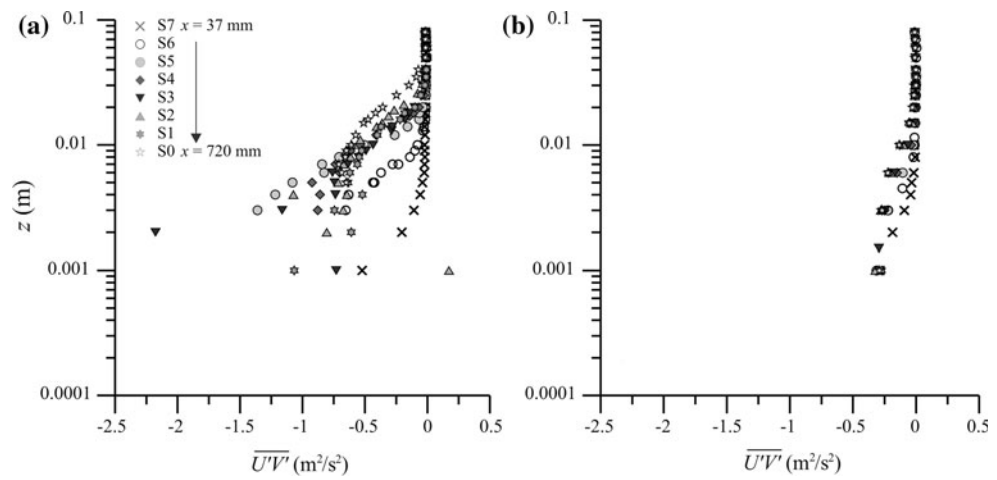


**Fig. 5** Measurements in air over water. Distribution of the mean turbulent Reynolds stresses in Section S2 ( $x = 520$  mm);  $U_\infty = 10.72$  m/s,  $u_* = 0.72$  m/s,  $\nu_{air} = 1.51 \times 10^{-5}$  m<sup>2</sup>/s. *dark square*,  $\overline{U'U'}$ ; *shaded circle*,  $\overline{V'V'}$ ; *diamond*,  $-\overline{U'V'}$ . The *dashed line* indicates the uniform tangential stress near the interface

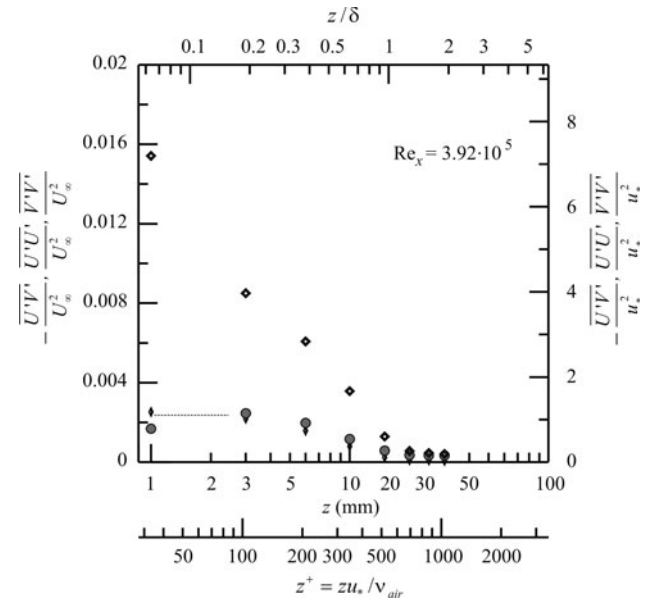


**Fig. 6** Measurements in air over a plane smooth rigid wall. Distribution of the mean turbulent Reynolds stresses in Section S2 ( $x = 520$  mm);  $U_\infty = 11.30$  m/s,  $u_* = 0.52$  m/s,  $\nu_{air} = 1.51 \times 10^{-5}$  m<sup>2</sup>/s. *Dark square*  $\overline{U'U'}$ , *shaded circle*  $\overline{V'V'}$ , *diamond*  $-\overline{U'V'}$

This value is 8 % larger than the friction velocity computed by fitting the mean horizontal velocity profile, which gives 0.52 m/s (Table 3). In this last case, the nearest point of measurement was at  $z^+ = 35$ , which was coincident with the upper limit of the buffer layer. Hence, the overestimation of the friction velocity can be considered as a consequence of the uncertainties in velocity measurements.

Another method for evaluating the ocean wind stress is the inertial dissipation technique (see, e.g., Yelland and Taylor 1996) but relevant in this respect is the analysis by Janssen (1999), who found that for large wind speed (in practice >15 m/s), observations of the surface stress by means of the inertial dissipation technique are so close to the surface that effects of growing ocean waves on the turbulent kinetic energy budget should be taken into account. This may give rise to an increase in the surface stress of 20 %. Correcting the kinetic energy budget by including the pressure term associated with growing waves gives considerable differences regarding the sea state dependence of the surface stress. For large winds, the drag coefficient increases compared to the standard inertial dissipation technique. Although the inertial dissipation technique is an appealing method, it also has its drawbacks because of the number of assumptions involved, and an empirical imbalance term is needed. The assumption that growing waves have no impact on the kinetic energy balance is also not justified.

### 3.2 Estimation of the effects of the gravity waves on turbulence within the air boundary layer

Waves modulate the air flow field by the crests and the troughs, i.e., to the coupling of the water waves and the air flow. An attempt to indirectly estimate the wave-induced component is based on the results by Hsu et al. (1981) who found that wave-induced flow generally has a spectrum different from the surface elevation spectrum, with the same fundamental component and several higher frequency harmonics but the magnitudes of the higher harmonics are negligible with respect to the fundamental mode (less than 10 %). By filtering the spectrum of the air flow according to the spectrum of the free surface elevation, the separation of the induced wave flow can be performed accurately.

Following Hsu and Hsu (1983), a critical height,  $z_c$ , can be defined as the location where  $U(z_c) = c$ , where  $c$  is the wave celerity. Hsu and Hsu (1983) used a wave-following frame where the origin of the vertical axis was at the instantaneous interface level. In a fixed frame, the critical height in a given section of the measurements varies with time. The critical height will tend towards infinity when  $U_\infty < c$ , whereas when  $U_\infty \gg c$ , the critical height is located very close to the interface, and the turbulent

boundary layer will be very similar to a boundary layer over a stationary wavy solid boundary, which corresponds to  $U_\infty/c \rightarrow \infty$  (there are several differences in the various mechanisms of turbulence generation and diffusion, see Longo 2012). This last condition was met in the present experiments because the wave celerity was a few tens of centimetres per second ( $c = 0.57\text{--}0.62$  m/s, computed by correlating the concurrent water level measurements in two different sections) and the wind speed was greater than 10 m/s. In the air-flow boundary layer, a modulation effect is due to separation, which begins a short distance behind the crest and reattaches on the front face of the next dominant wave, as shown by Chang et al. (1971).

To quantify the intrusion of water waves in the air boundary layer close to the interface, it can be assumed that the flow field influenced by the water waves has energy only in the frequency range of the water waves, whereas turbulence is characterised by higher frequencies. The water level analysis revealed that the dominant waves had a frequency of  $\sim 7$  Hz in all sections except for Sects. 6 and 7, where they reached  $\sim 9$  and  $\sim 16$  Hz, respectively. This frequency shift is due to non-linear, wave-wave transfer and coalescence; the long waves (with a larger period) move faster and capture the short waves (with a shorter period). Low-pass filtering of the instantaneous air velocity allows the separation of the oscillating components associated with the water waves and the fluctuations due to turbulence. The results are approximate, as they are affected by the chosen cut-off frequency.

In Figs. 7, 8 and 9, the profiles of the wave-induced stress and turbulence are shown. Near the domain where water waves are present, turbulence is significantly damped, and the air flow field is dominated by the wave-induced component, which is more evident for the horizontal velocity and less evident for the vertical velocity. The shear stress close to the water waves is almost uniform, and the turbulent contribution is negligible in this region. Note that the tangential stress becomes positive at the last point of measurement; this result is not very accurate because the data rate is very low at this point, but follows similar findings by Anisimova et al. (1982) and Shaikh and Siddiqui (2011a). In general, it is expected that very close to the interface, waves exert shear stress on the overlying air.

The behaviour was similar for all sections. The best scaling length for the wave-induced flow is  $H_{\text{rms}}$ . Figure 10 shows the wave-induced tangential stresses at all sections, which becomes negligible more than  $5 H_{\text{rms}}$  above the still water level. This result is consistent with Shaikh and Siddiqui (2011a) results, who found that at heights greater than three significant wave height from the water surface, the magnitude of wave-induced velocity is negligible. The wave statistics of the present tests indicate a ratio  $H_{1/3}/H_{\text{rms}}$

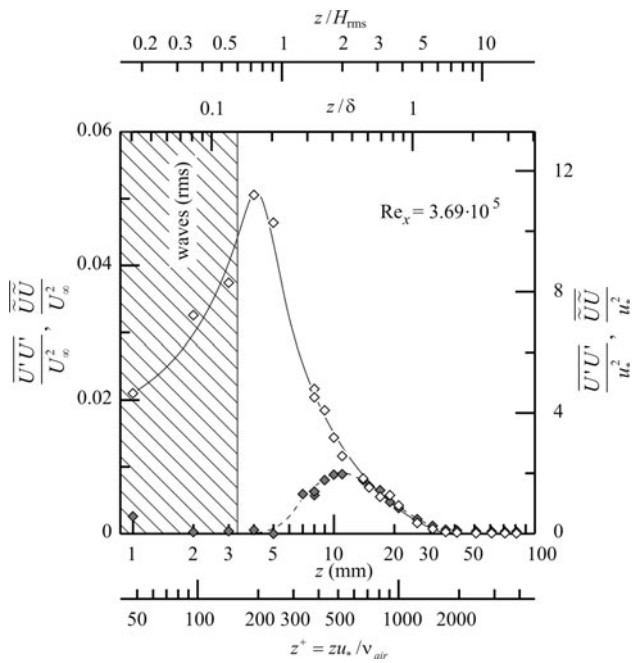


**Fig. 7** Measurements in air over water. Distribution of the mean turbulent and oscillating horizontal Reynolds stresses in Section S2 ( $x = 520$  mm);  $U_\infty = 10.72$  m/s,  $u_* = 0.72$  m/s,  $H_{rms} = 5.4$  mm,  $\nu_{air} = 1.51 \times 10^{-5}$  m<sup>2</sup>/s. Shaded square  $\overline{U'U'}$ , open square  $\overline{\tilde{U}\tilde{U}}$ , bold line and dashed line are fitting curves

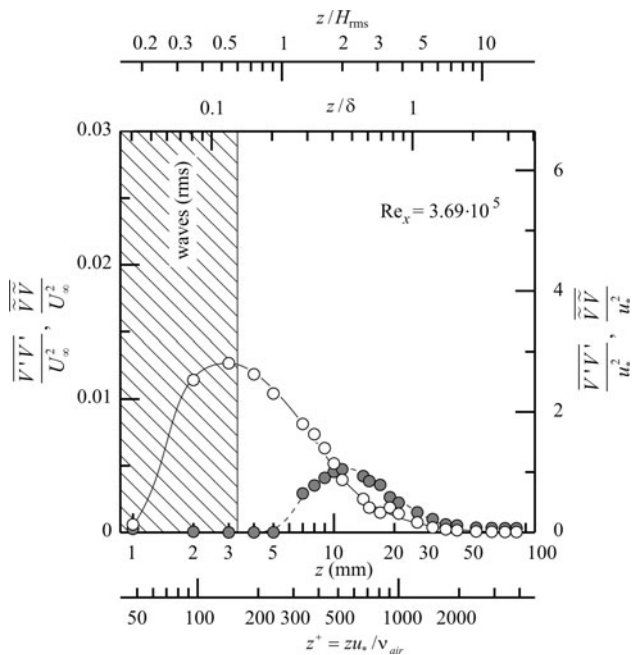


**Fig. 8** Measurements in air over water. Distribution of the mean turbulent and oscillating vertical Reynolds stresses in Section S2 ( $x = 520$  mm);  $U_\infty = 10.72$  m/s,  $u_* = 0.72$  m/s,  $H_{rms} = 5.4$  mm,  $\nu_{air} = 1.51 \times 10^{-5}$  m<sup>2</sup>/s. Shaded circle  $\overline{V'V'}$ , open circle  $\overline{\tilde{V}\tilde{V}}$ , bold line and dashed line are fitting curves

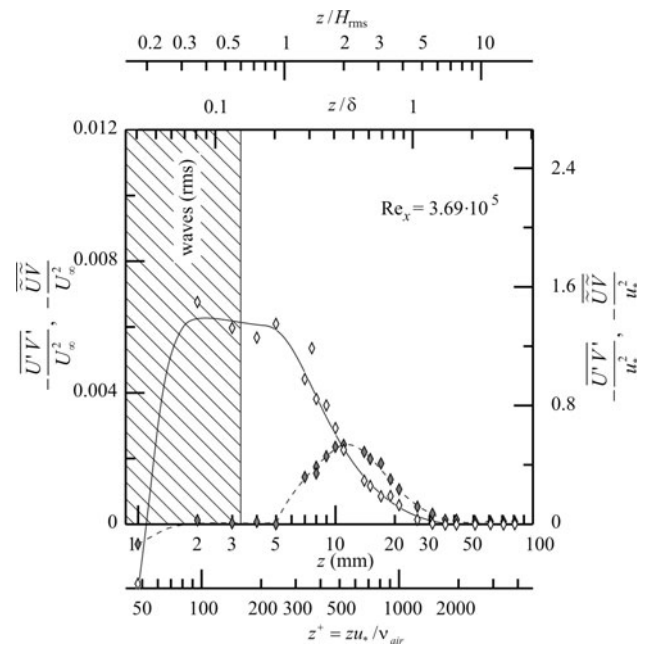


**Fig. 9** Measurements in air over water. Distribution of the mean turbulent and oscillating Reynolds stresses in Section S2 ( $x = 520$  mm);  $U_\infty = 10.72$  m/s,  $u_* = 0.72$  m/s,  $H_{rms} = 5.4$  mm,  $\nu_{air} = 1.51 \times 10^{-5}$  m<sup>2</sup>/s. Shaded square  $-\overline{U'V'}$ , open square  $-\overline{\tilde{U}\tilde{V}}$ , bold line and dashed line are fitting curves

~1.5. In this context, it is pertinent to the work of Shaikh and Siddiqui (2011b) that shows that the waves over which the flow separation occurs (similar to the waves of present experiments) are steeper and larger in amplitude than the waves with no flow separation and that the influence of flow separation is mainly restricted on the crest-to-trough region. The turbulence is significantly enhanced within the separation zone and the separated flow enhances the downward momentum transfer on the leeward side and in the trough. The trends remain almost the same for the separated and non-separated flows, but the flow separation enhances the magnitudes of the wave-induced properties within the distance of one to two significant wave heights from the water surface.

Also, relevant is the analysis by Sjöblom and Smedman (2002) who show that there is an imbalance between normalised production and normalised dissipation, also in neutral conditions, and that this imbalance depends not only on stability but also on wave age and wind speed. For small wave ages and high wind speeds, production is larger than dissipation at neutral conditions. For saturated waves and moderate wind speeds, the sea surface resembles a land surface, while for swell and low wind speeds, dissipation strongly exceeds production. The small wave age and high wind speed is the condition of the present experiments, even though we are not able to quantify the TKE budget in order to verify the forecast behaviour (production larger than dissipation).

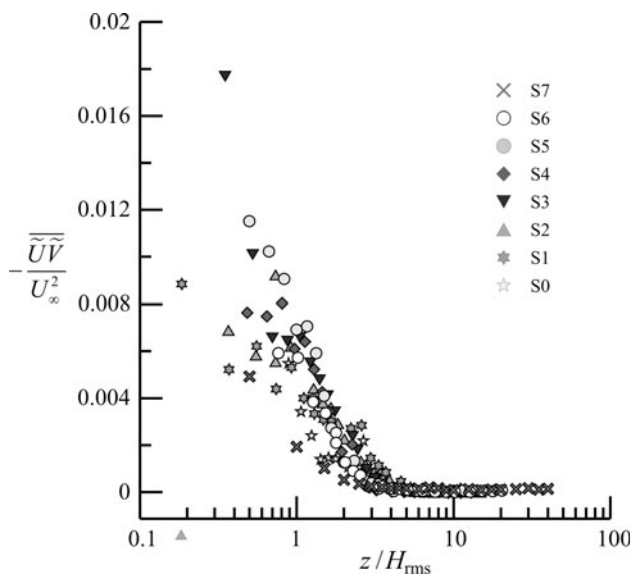


**Fig. 10** Measurements in air over water. Distribution of the oscillating tangential stresses

In a subsequent paper, Sjöblom and Smedman (2003) propose a division of the lower part of the boundary layer into three height layers: (1) a wave-influenced layer close to the surface, (2) a transition layer and (3) an undisturbed ‘ordinary’ surface layer; the depth of the layers is determined by the wave state. Their analysis classifies the waves in growing waves if  $c/U_{10}\cos\theta < W_{\text{grow}}$ , mature or saturated waves, if  $W_{\text{grow}} < c/U_{10}\cos\theta < 1.2$ , and swell if  $c/U_{10}\cos\theta > 1.2$ .  $U_{10}$  is the reference wind speed at the height of 10 m,  $\theta$  is the angle between wind and wave direction and  $W_{\text{grow}}$  is a parameter having value 0.5–0.9. The height structure cannot, however, be found for the normalised dissipation, which is only a function of the stability, except during pronounced swell where the actual height also has to be accounted for. The results have implications for the height variation of the turbulent kinetic energy (TKE) budget. Thus, the imbalance between production and dissipation will also vary with height according to the variation of wave state. Assuming the reference wind speed coincident with the asymptotic wind speed, all the waves of the present experiments are growing having an age at most equal to 0.050.

#### 4 Intermittency

For shear flows over a boundary, the edge of the turbulent boundary layer is not sharp. There is an overlap region where turbulence becomes intermittent. Intermittency in turbulence was documented for the first time by Townsend (1948). After checking that the distribution,  $p(U')$ , of the probability density of the velocity fluctuation in a fully

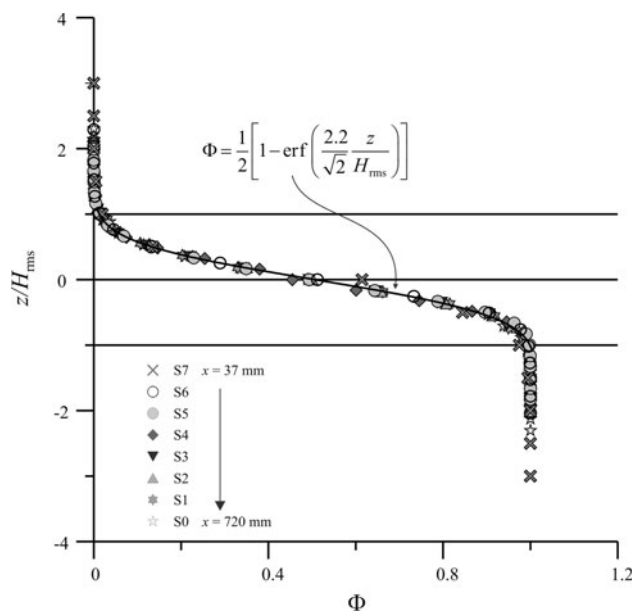


**Fig. 11** Water concentration profiles

turbulent flow is Gaussian, a higher kurtosis will indicate that most of the variance is due to infrequent extreme deviations. The kurtosis is computed as:

$$F = \frac{\int_{-\infty}^{+\infty} U'^4 p(U') dU'}{\left[ \int_{-\infty}^{+\infty} U'^2 p(U') dU' \right]^2} = \frac{\overline{U'^4}}{\left( \overline{U'^2} \right)^2}. \tag{5}$$

The intermittency factor is defined as the ratio of the kurtosis of the velocity (or its time derivative) in the turbulent region to that in the intermittent region:

$$\gamma = \frac{3}{F} \equiv \frac{3}{\overline{U'^4} / \left( \overline{U'^2} \right)^2}. \tag{6}$$

The kurtosis is equal to 3 in a fully turbulent region (Gaussian probability density) and is greater than 3 in the intermittent region; as a consequence, the intermittency factor decreases from near the boundary to the free stream. Then, the kurtosis tends to increase again in the free stream, where external turbulence dominates. For this last reason, it is convenient to weigh the probability density function of the free stream against that inside the boundary layer using the relative turbulence levels.

In the presence of waves, intermittency is also influenced by the presence and absence of water, i.e., by the water concentration. Using the water level measurements, the water concentration,  $\Phi$ , can be computed. Curve fitting was performed based on the normal distribution of the free surface elevation (Fig. 11):

$$\Phi = (0.506 \pm 0.04) \left( 1 - \text{erf} \left[ (1.58 \pm 0.04) \frac{z}{H_{\text{rms}}} \right] \right), \tag{7}$$

for  $-H_{\text{rms}} < z < H_{\text{rms}}$

with coefficients computed at the 95 % level of confidence. The expression can be approximated as:

$$\Phi = \frac{1}{2} \left[ 1 - \operatorname{erf} \left( \frac{2.2}{\sqrt{2}} \frac{z}{H_{\text{rms}}} \right) \right], \quad \text{for } -H_{\text{rms}} < z < H_{\text{rms}}, \tag{8}$$

which is similar to the expression found for the free surface fluctuations generated by a Crump weir in a flume (Longo 2010).

With this simple approach, it can be assumed that the effect of the water–air interface is similar to the effect of a boundary between turbulent and non-turbulent motion.

The curves in Fig. 12a and b show the computed intermittency factor in air over water and in air over a plane smooth rigid wall, respectively. The dashed curve is a Gaussian integral curve expressed by the following equation:

$$\gamma = \frac{1}{2} (1 - \operatorname{erf} \zeta), \quad \text{where } \zeta = \left( \sqrt{2} \frac{\sigma}{\delta} \right)^{-1} \left[ \frac{z}{\delta} - 0.78 \right]$$

$$\text{and } \left( \sqrt{2} \frac{\sigma}{\delta} \right)^{-1} = 5 \rightarrow \sigma = 0.14\delta \tag{9}$$

Equation (9) is given by Klebanoff (1955) for a zero-pressure-gradient boundary layer and represents the variation of the intermittency factor  $\gamma$  with the distance from the wall. Such distribution indicates that the edge of the boundary layer has a random character with a mean position at  $z/\delta = 0.78$  and which rarely extends outside the region  $z/\delta = 0.4\text{--}1.2$ .

Near the interface the presence or absence of water mimics an intermittency due to the absence of validated velocity signal if water is present (the geometry of the LDV setup allows measurements only in air). Hence, plotting the computed air concentration equal to  $1 - \Phi$  ( $\Phi$  is the water concentration) results in a turbulence intermittence, which can explain only part of the measured intermittency factor.

The dashdot curves in Fig. 12a) represent the correction due to the measured water concentration in the two end sections of measurements. There is still a missing part of intermittency, which can be attributed to a periodic re-laminarisation of the air boundary layer induced by the waves; the air-flow boundary layer was modulated by the trough-crest series, and the turbulence was locally damped. Only the data from Sections S0 and S7 are shown; the results for the other sections are a transition between the results at these end sections.

### 5 Quadrant analysis

To reveal the structure of turbulence, Reynolds shear stresses contributions are categorised according to their origin and divided into four quadrants. Then, conditionally sampling according to the quadrant gave the statistics of the events classified, as shown in Fig. 13.

Ejections and sweeps are generally the main contributors to the transfer of momentum in the turbulent boundary layer. The event-averaged shear stress for the  $i$ th quadrant is computed as:

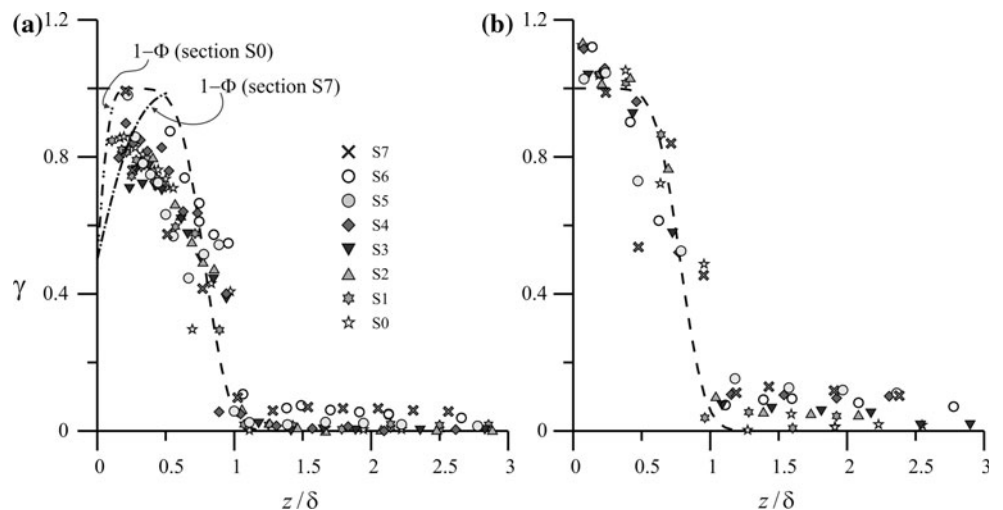
$$\langle \overline{U'V'} \rangle_i = \frac{1}{N_i} \sum_{j=1}^{N_i} [U'V'_j]_i \quad \text{for } i = 1, \dots, 4, \tag{10}$$

where  $N_i$  is the number of events in the  $i$ th quadrant and  $j$  is the current sample number. The average shear stress for the  $i$ th quadrant is

$$\overline{U'V'}_i = \frac{1}{N} \sum_{j=1}^{N_i} [U'V'_j]_i \quad \text{for } i = 1, \dots, 4. \tag{11}$$

The ratio,  $N_i/N$ , is the relative permanence of the events in the  $i$ -quadrant, hence

**Fig. 12** Distributions of the intermittency factor. **a** Measurements in air over water; **b** measurements in air over a plane smooth rigid wall. *Dashed curve* Gaussian integral function by Klebanoff (1955) for a zero-pressure-gradient boundary layer over a rigid smooth wall. *Dot-dashed curves* Air concentration for measurements in Sections S0 and S7



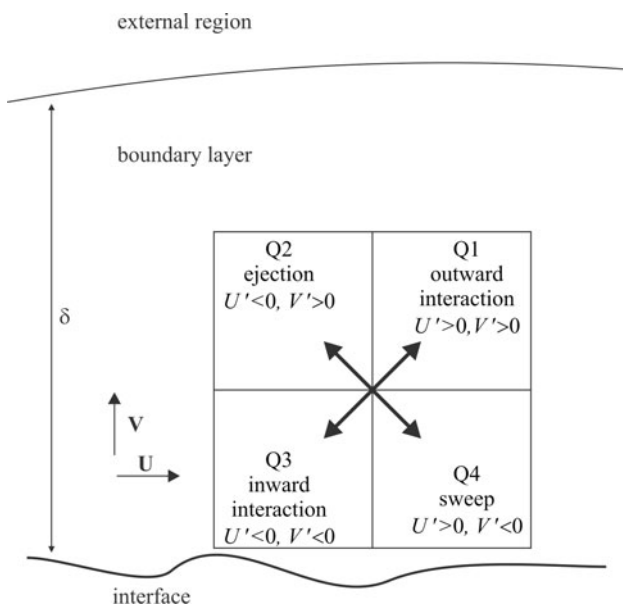


**Fig. 13** Quadrant decomposition of the fluctuating components of the velocity

$$\overline{U'V'}_i = \frac{N_i}{N} \langle \overline{U'V'} \rangle_i \tag{12}$$

and the total shear stress is

$$\overline{U'V'} = \sum_{i=1}^4 \overline{U'V'}_i. \tag{13}$$

We can further limit the data by considering only values above a fixed amplitude threshold, i.e., satisfying the relation  $|U'V'| > T$ , where  $T$  is usually defined in terms of the root mean square stress:

$$|U'V'| > H(U'_{rms}V'_{rms}), \tag{14}$$

where  $H$  is a threshold with the magnitude of unity. We can also define the concentration of the  $i$ th quadrant for a fixed threshold level:

$$C_H^i = \frac{1}{N} \sum_{j=1}^N \phi_{H,j}^i, \tag{15}$$

where

$$\phi_{H,j}^i = \begin{cases} 1 & \text{if } |U'V'|_j > TH \text{ and belongs to the } i - \text{quadrant} \\ 0 & \text{otherwise} \end{cases} \tag{16}$$

The sum,  $\sum_{i=1}^4 C_H^i$ , is the concentration of stress satisfying relation (Eq. 15). We can also consider the phasic-averaged Reynolds stress for the  $i$ th quadrant:

$$\left( \widehat{U'V'} \right)_H^i = \frac{\sum_{j=1}^N (U'V')_j \phi_{H,j}^i}{\sum_{j=1}^N \phi_{H,j}^i} \tag{17}$$

and the time-averaged Reynolds stress for the  $i$ th quadrant:

$$\left( \overline{U'V'} \right)_H^i = \frac{1}{N} \sum_{j=1}^N (U'V')_j \phi_{H,j}^i = C_H^i \left( \widehat{U'V'} \right)_H^i. \tag{18}$$

The results here discussed refer to fluctuating velocities including the wave-induced contribution, as expressed by Eq. (2). The Reynolds shear stress measurements for the wind above water are shown in Fig. 14a) for Section S2. The data show the extent to which each quadrant contributes to the overall stress in a time-averaged sense. The second quadrant (ejection) peaks at  $z/\delta = 0.4$ , whereas the fourth quadrant (sweep) peaks at  $z/\delta = 0.15$ . The other two quadrants (inward and outward interaction) provide minor contributions and peak at  $z/\delta = 0.1-0.2$ . The peaks for ejections and sweeps are 3 and 4 times greater than those in quadrants 1 and 3. This value is larger than the value  $\approx 2$  reported in Foster et al. (2006).

In Fig. 14b, the concentration is shown for the Reynolds stress and the quadrant contributions, where they all peak at  $z/\delta = 0.1$  and reach minimum at  $z/\delta = 1$ . Near the wave crests the overall contribution of the sweeps plus ejections is nearly equal to 66 %, similar to the value observed in Foster et al. (2006). Then, at higher level, the ejections still dominates, whereas the sweeps progressively reduce their frequency. This behaviour is different from the results by Foster et al. (2006) that show a dominant presence of the sweeps but with a limited intensity. In the outer stream, the external limited turbulence resulted in relatively high concentration values but a very limited Reynolds stress.

In Fig. 15, the quadrant maps for the fluctuating components of the velocity in three sections are shown at various vertical levels in the form of joint probability distribution functions (p.d.f.) of  $U'$  and  $V'$  normalised by the free stream velocity. The darkest regions correspond to the greatest concentration of fluctuations. Near the edge of the boundary layer, turbulence was limited and appeared to be isotropic (at least in the vertical plane), with equal Reynolds shear stress in the four quadrants. Then, moving towards the interface, the joint p.d.f. becomes elliptic, with a maximum in the Q4 quadrant (sweep) except for a small fetch in Section S4. The variation of the shape of the p.d.f. begins at  $z/\delta = 0.5$ . A long tail is present in Q2 (ejection) and, generally, the streamwise fluctuations are larger than the vertical ones despite being not as dominant as in a boundary layer over a rigid wall (see Nolan et al. 2010). A different view is shown in Fig. 16, where the quadrant contributions to the Reynolds shear stress and the global contribution for a fixed threshold ( $H = 1$ ) are presented at all fetches. Note that the ejections and sweeps are one order of magnitude larger than the inward and outward interactions and that the range of the contour plots is different. The most evident contributions by the ejections and the

**Fig. 14** Measurements in air over water, Section S2. **a** Time-averaged Reynolds shear stress with threshold  $H = 1$  (filled circle) and quadrant decomposed; **b** concentration. open circle Q1 (outward interaction), open square Q2 (ejection), dark square Q3 (inward interaction), triangle Q4 (sweep)

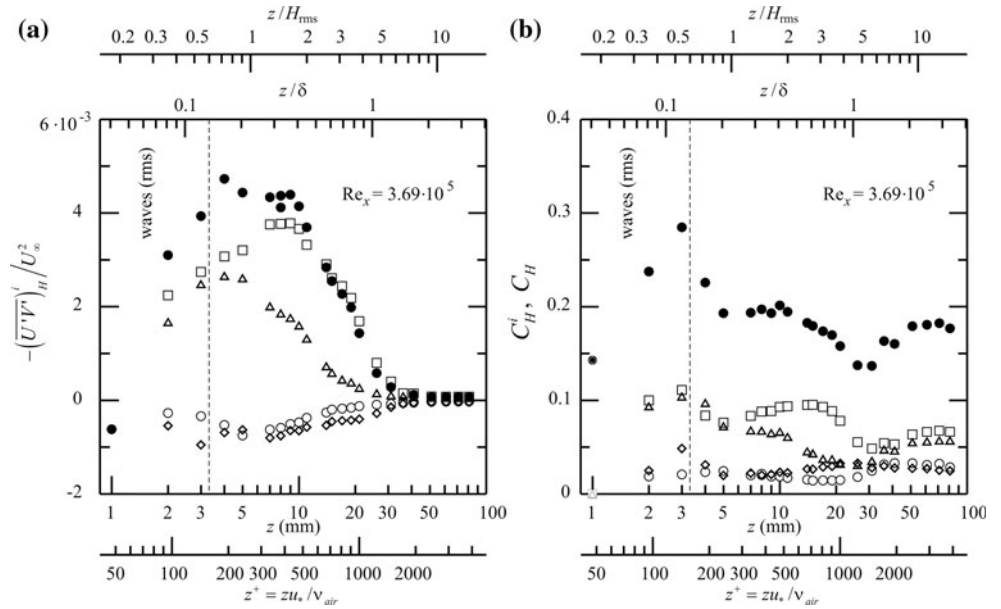
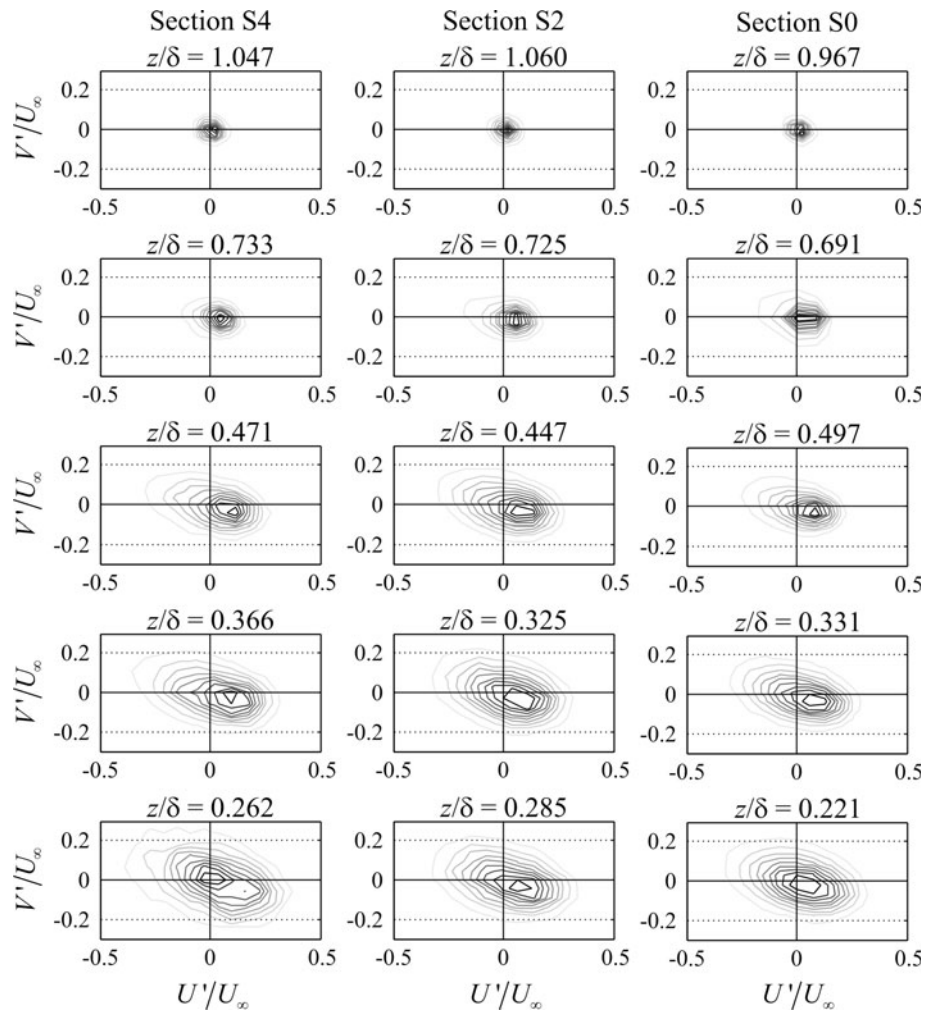


**Fig. 15** Joint p.d.f. for the fluctuating velocities in Sections S4, S2 and S0 (increasing fetch) at the noted positions in the vertical direction



sweeps are near the interface, at  $z/\delta < 0.2$ . At small fetches ( $x < 0.3$  m), bursting is stronger except for the outward interaction (Q1), which reaches its maximum value at intermediate fetches ( $x \approx 0.5$  m).

Figure 17 shows the contour map with the results of the quadrant analysis and without quadrant separation for Section S4. Each subfigure gives the data for one quadrant at increasing thresholds  $H$  ( $x$ -axis), and the vertical distance is normalised by the local boundary layer thickness. The shaded area represents the Reynolds shear stress non-

dimensionalised by the asymptotic wind velocity, and the contour lines represent the duration fraction (the concentration). The duration fraction contour lines indicate the fraction of time for the existence of the Reynolds shear stress, which exhibited an intensity proportional to the grey scale. The phasic-averaged Reynolds shear stress is equal to the ratio of the time-averaged Reynolds shear stress and duration fraction. A small time-averaged shear stress with a very short duration indicates an intense turbulent spot, i.e., a large phasic-averaged value. All the contributions were

**Fig. 16** Measurements in air over water. Upper panels time-averaged Reynolds shear stress quadrant decomposed with threshold  $H = 1$  for the experimental domain. Contour lines increment from 0 to  $-0.001$  in 0.0001 steps for Q1 and Q3, from 0 to 0.01 in 0.001 steps for Q2 and Q4. Contributions from Q1 and Q3 were negative and one order of magnitude smaller than contributions from Q2 and Q3. (Note that the grey colour bar is scaled differently.) In the lower panel, the time-averaged Reynolds shear stress without quadrant decomposition is shown, with contour line increments from 0 to 0.01 in 0.001 steps

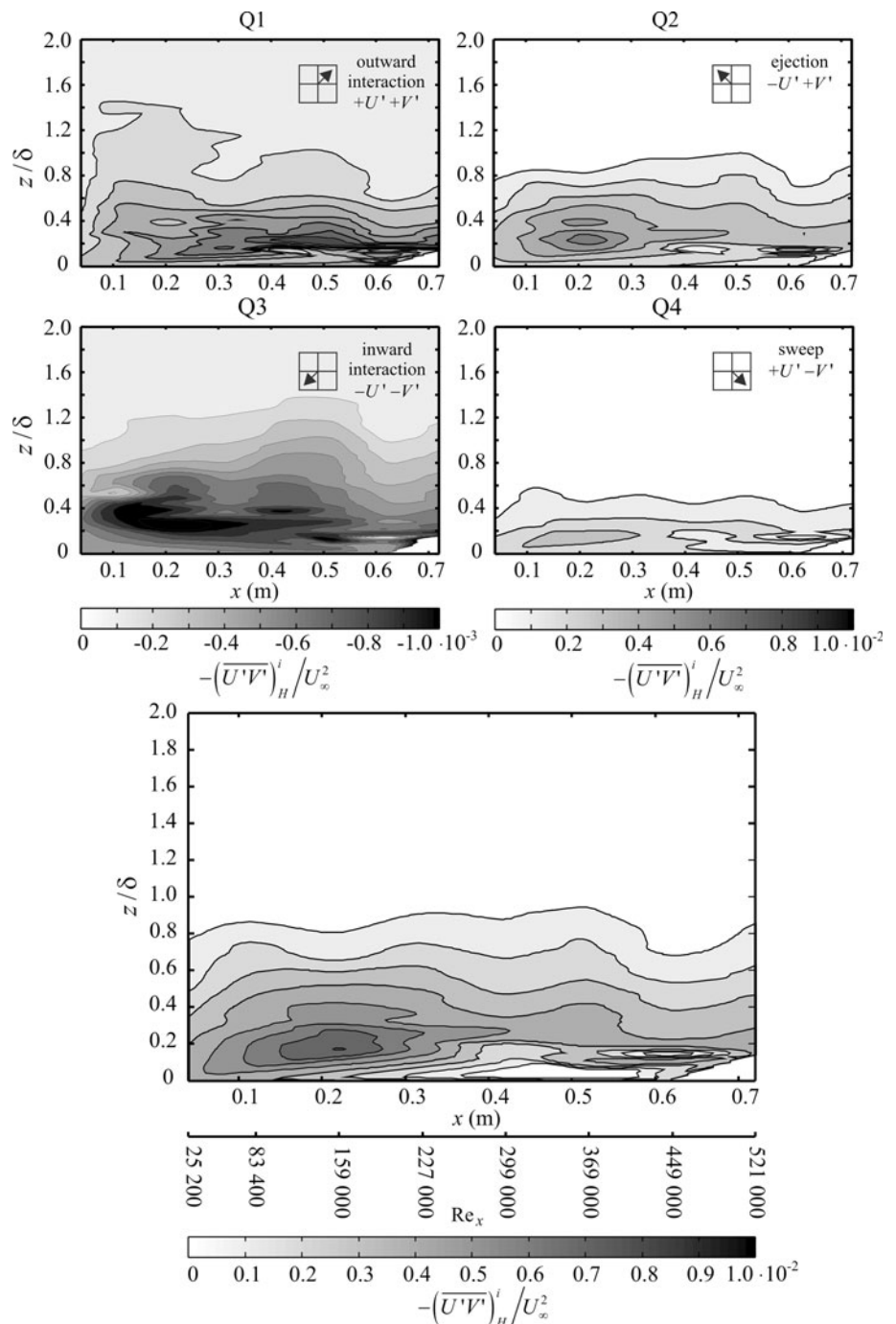
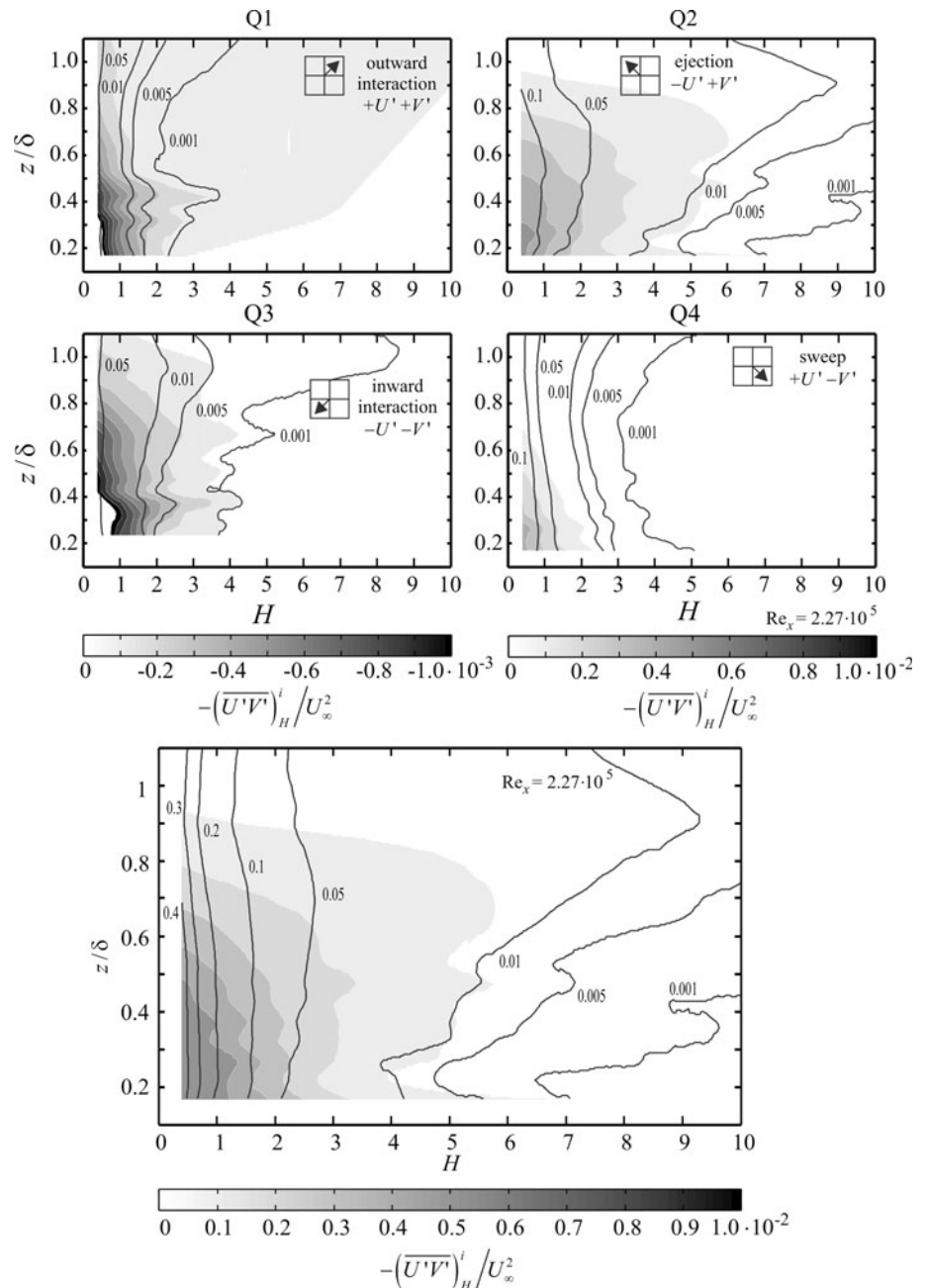


**Fig. 17** Measurements in air over water, Section S4. Time-averaged Reynolds shear stress in each quadrant decomposed (*upper panels*) and without decomposition (*lower panel*) with increasing threshold  $H$  (note that the *grey colour bar* is scaled differently). The *isolines* of duration fraction are superimposed



intense at the upper limit of the boundary layer and in the lower half-layer. Similar results are presented in Figs. 18 and 19 for Section S2–S0.

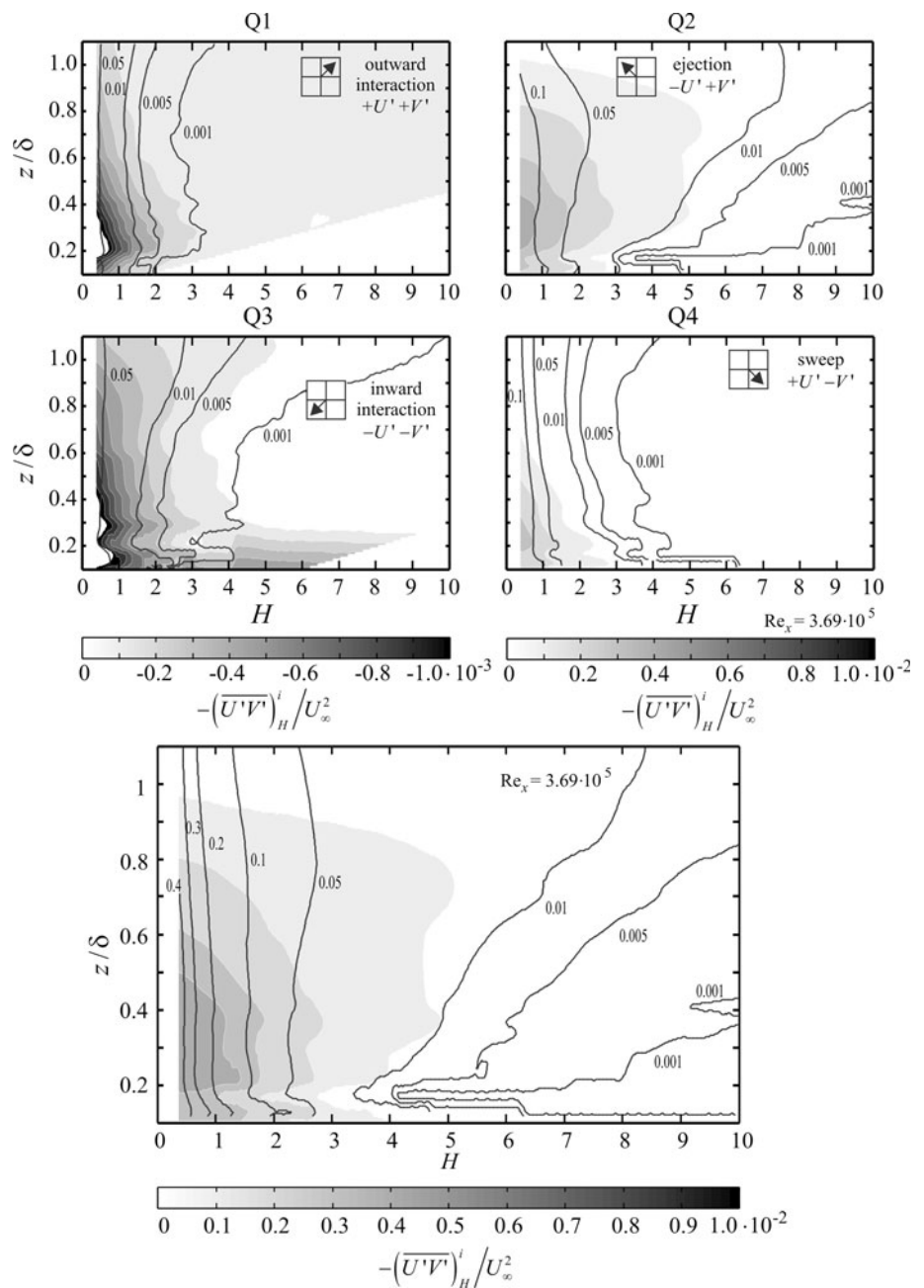
In Section S4, the duration of the sweeps (Q4) is almost constant in the vertical direction and inversely proportional to the threshold  $H$ , where the maximum time-averaged values are in the lower part of the boundary layer. Ejections (Q2) generally last longer than sweeps and for increasing thresholds, reached the maximum value in the middle of the boundary layer, with a duration fraction reduced from  $\sim 10$  to  $\sim 1$  %, whereas the relative intensity (normalised by the asymptotic wind speed) decreases from  $\sim 5 \times 10^{-3}$

to  $\sim 10^{-3}$ . The correspondent deficit can be observed in the outward interactions (Q1), i.e., large-amplitude positive streamwise perturbations, which means that large-amplitude negative streamwise perturbations are preferentially lifted.

A similar behaviour was observed in Section S2. The pattern was different than Section S0, where ejections and sweeps are concentrated close to the water interface.

Figure 20 shows the quadrant analysis of the vertical momentum flux in the surface layer (air side) for varying wave age. The panels refer to measurements in Sections S7–S0, characterised by increasing wave celerity for a

**Fig. 18** Measurements in air over water, Section S2. Time-averaged Reynolds shear stress in each quadrant decomposed (*upper panels*) and without decomposition (*lower panel*) with increasing threshold  $H$  (note that the *grey colour bar* is scaled differently). The *isolines* of duration fraction are superimposed

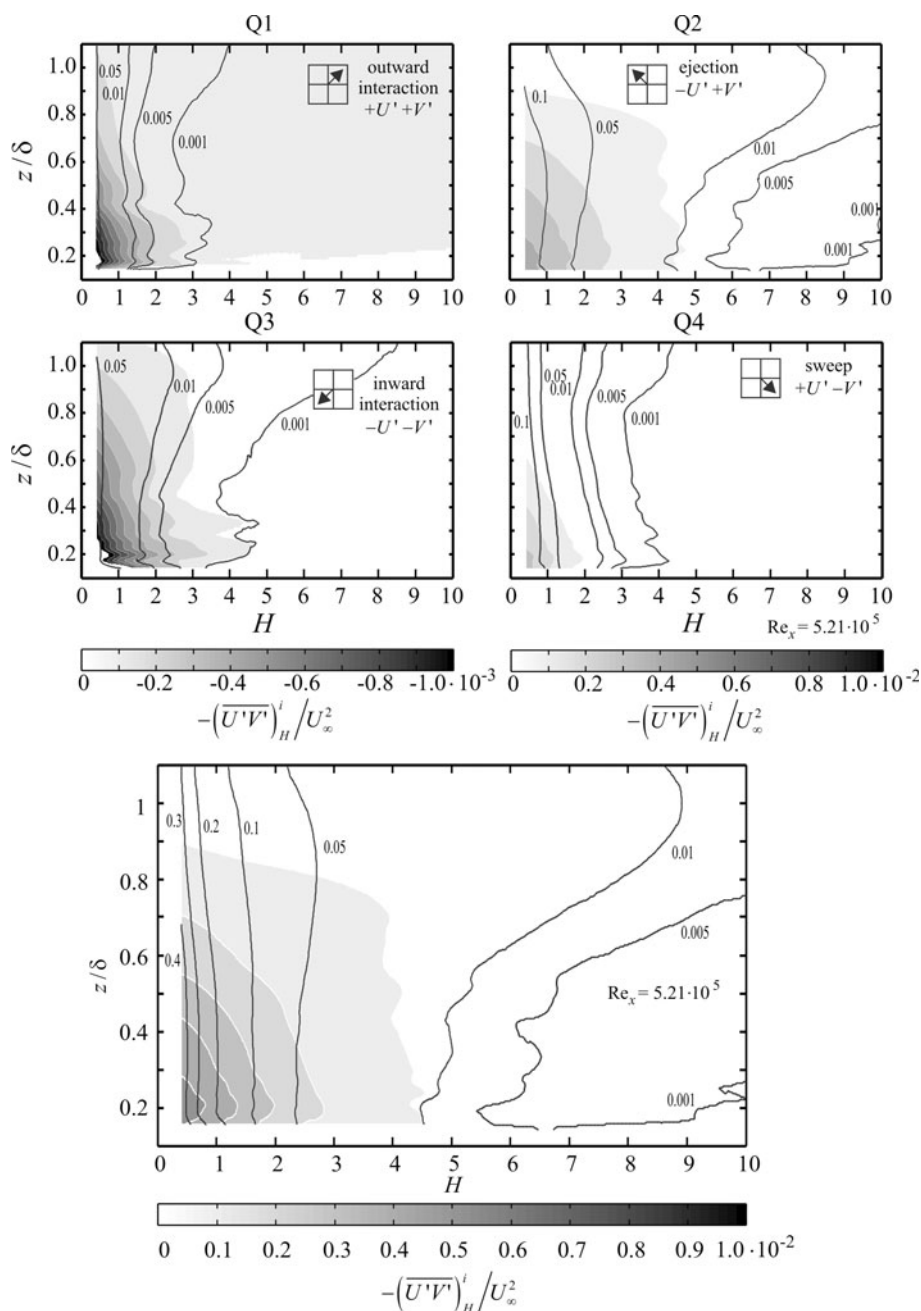


given asymptotic wind speed, i.e., by increasing maturity of the water waves. The vertical axis reports the level of non-dimensional measurements with respect to the r.m.s. height of the water waves, the horizontal axis reports the ratio between the sweep-ejection events and the outward-inward interaction. According to Sullivan et al. (2008), under low winds the fast-moving components of the wave field enhance the upward momentum transport from the ocean to the atmosphere (this momentum appears in the positively signed flux quadrants Q1, Q3). At a sufficiently large wave age a near balance between negative and positive flux contributions is reached, implying zero

surface drag. The quadrant momentum flux distributions are a consequence of competing effects; fast-moving waves generate positive momentum flux while small slow-moving waves act similar to conventional roughness elements.

The observed values in the present experiments are much larger than those observed for relatively mature waves, usually smaller than 2.0 (see Fig. 16 in Sullivan et al. 2008), peak near  $z = H_{rms}$  with a progressive reduction moving towards the external region, far from the free surface. They are also larger than the value  $\approx 2.6$  recorded for stationary roughness (wave age = 0, also in Fig. 16 in Sullivan et al. 2008).

**Fig. 19** Measurements in air over water, Section S0. Time-averaged Reynolds shear stress in each quadrant decomposed (*upper panels*) and without decomposition (*lower panel*) with increasing threshold  $H$  (note that the *grey colour bar* is scaled differently). The *isolines* of duration fraction are superimposed



## 6 Turbulence production

The rate of energy transfer from the mean flow to turbulence is considered a production term and is given by

$$P = -\overline{U'V'} \frac{\partial U}{\partial z}. \quad (19)$$

The proper scaling is through the boundary layer thickness,  $\delta$ , and the freestream velocity,  $U_\infty$ . For flow over water (Fig. 21a), the energy transfer is confined to the boundary layer and reaches a maximum at  $z/\delta \simeq 0.2$ . The

distribution is similar to that of a self-preserving boundary layer with a relatively strong positive-gradient pressure, but the maximum intensity is much larger. No evidence of negative production (i.e., transfer from turbulence to mean flow) is present.

For flow over a plane smooth rigid wall (Fig. 21b), the distribution is similar to a self-preserving boundary layer, with minor differences in the domain of  $0.1 < z/\delta < 0.2$ , which can be attributed to a very small, positive-gradient pressure in the present experimental boundary layer. In fact, the effect of a positive-gradient pressure is an

**Fig. 20** Quadrant analysis of the vertical momentum flux for varying age with wind-following waves. The plots refer to the 8 sections of measurements

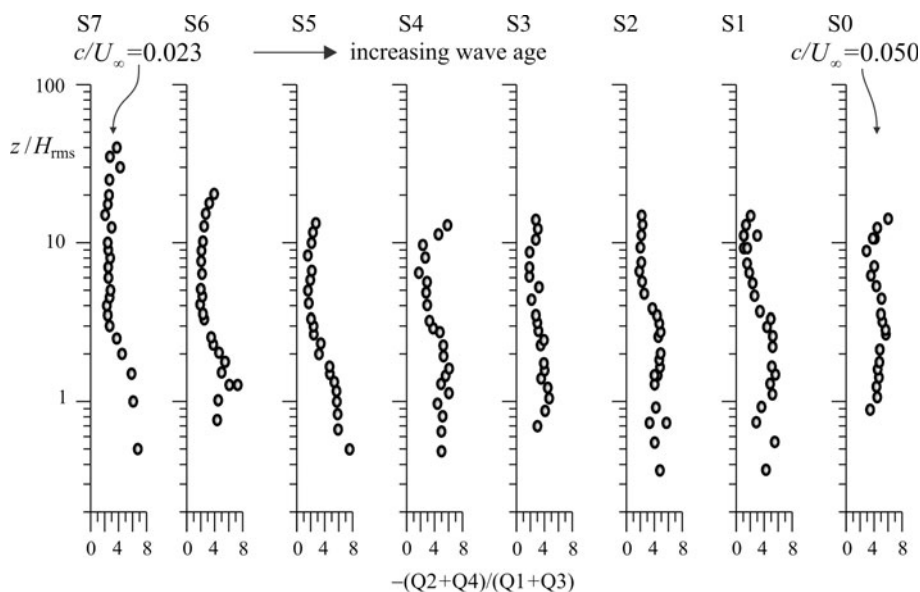
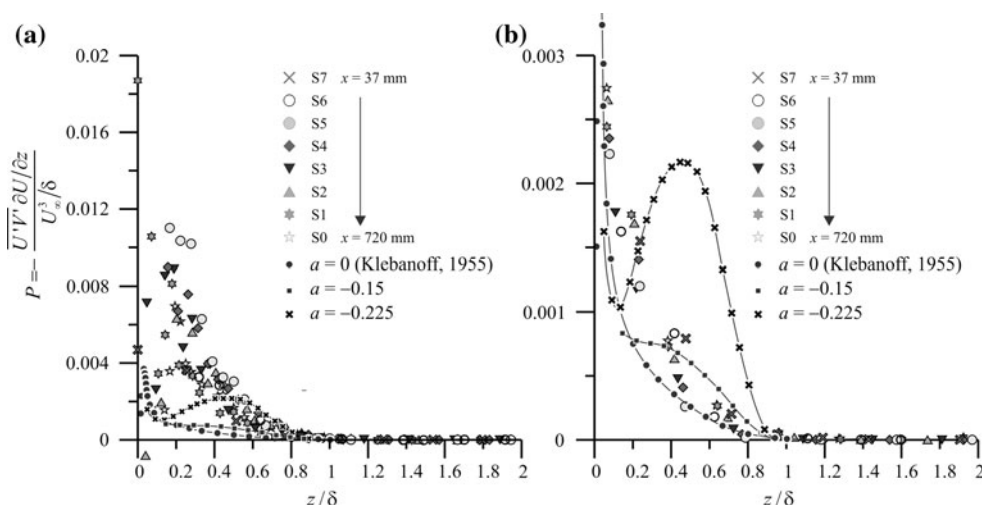


**Fig. 21** Distributions of the mean turbulent energy production. **a** Measurements in air over water; **b** measurements in air over a plane smooth rigid wall. The data by Klebanoff (1955) refer to a self-preserving boundary layer with a zero-pressure gradient. The other data refer to a boundary layer with a free stream velocity,  $U_\infty \propto (x - x_0)^a$



enhanced uniformity of production in the whole boundary layer (Townsend 1976) instead of a peak very close to the buffer layer. For comparison, the zero-pressure-gradient boundary layer distribution (Klebanoff 1955) and two positive-gradient-pressure boundary layer distributions ( $a = -0.15$  and  $a = -0.225$ ), where  $a$  is the exponent of the velocity variation with the fetch,  $U_\infty \propto (x - x_0)^a$  are shown.

It is also interesting to quantify the contribution to TKE by bursts, eventually separated in quadrants. We define

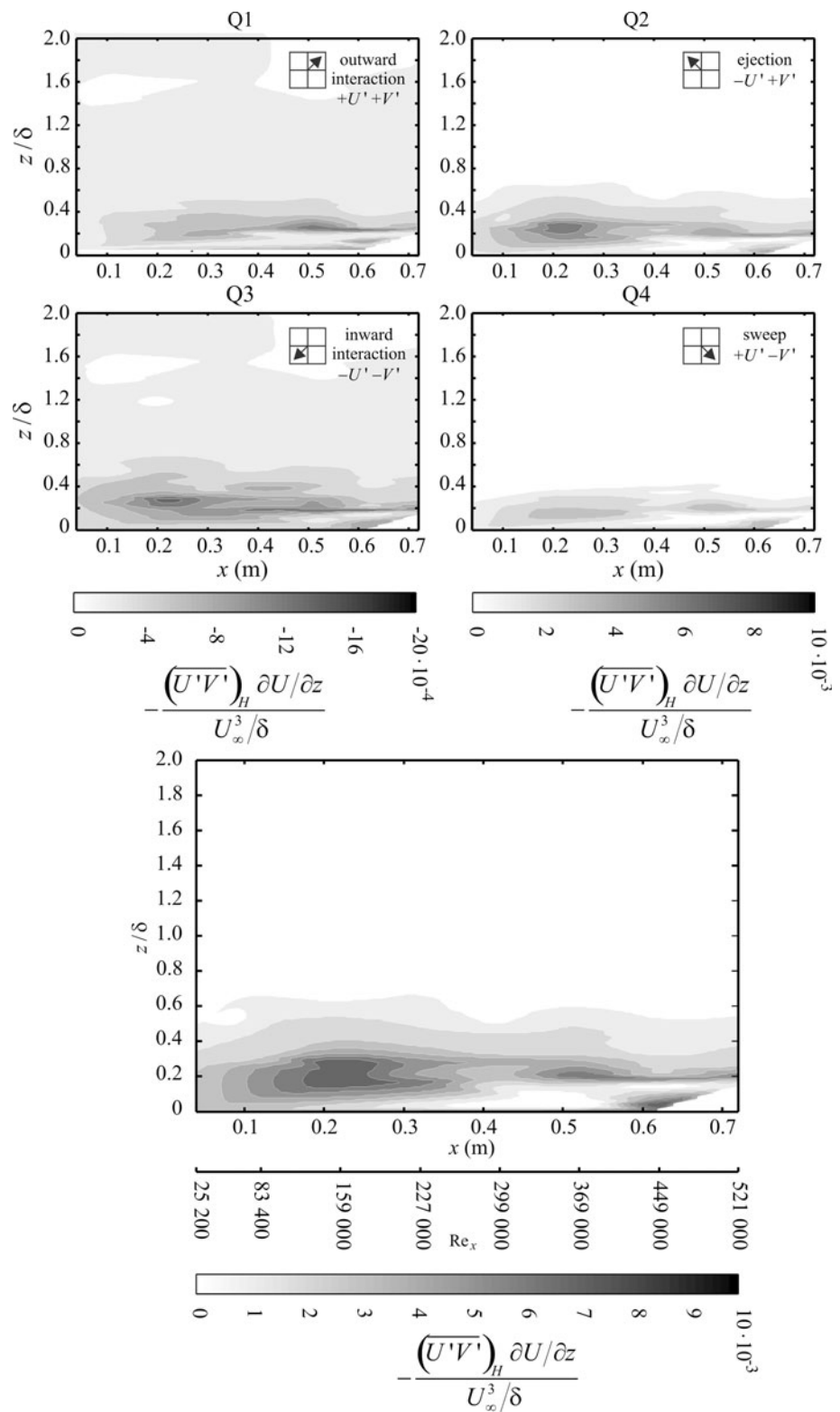
$$P_H^i = -(\overline{U'V'})_H^i \frac{\partial U}{\partial z}, \quad (20)$$

which is the contribution of turbulent spots with threshold  $H$  in the  $i$ -quadrant, and

$$P_H = \sum_{i=1}^4 P_H^i \quad (21)$$

is the contribution of turbulent spots with threshold  $H$  for all quadrants. Figure 22 shows a contour plot of the TKE production by turbulent spots across the experimental domain, where in the abscissa, the local Reynolds number is also reported. The values are non-dimensionalised by  $U_\infty$  and  $\delta$ , and peak at  $z/\delta = 0.2$  with  $Re_x = 3.7 \times 10^5$ . A significant contribution starts from  $Re_x = 3 \times 10^5$ , after which a spatial periodicity is observed, as though cells of intense turbulence spots are present. The quadrant decomposition gives similar results, with ejections much more efficient than sweeps. The inward and outward interactions (Q1 and Q3) give a negative contribution but are almost one order of magnitude smaller than the positive contribution (the grey scale is different for Q1–Q3 and Q2–Q4). These results can be compared with the results from Nolan et al. (2010), who found dominant activity in the inner half of the boundary layer (close to the wall), but

**Fig. 22** Measurements in air over water. Time-averaged production of turbulent kinetic energy by the Reynolds shear stress of each quadrant decomposed (*upper panels*) and without decomposition (*lower panel*) with threshold  $H = 1$  for the experimental domain. Contour line increments are from 0 to  $-0.002$  in  $0.0002$  steps for Q1 and Q3 (contributions for Q1 and Q3 are negative, note that the grey colour bar is scaled differently). Contour line increments are from 0 to  $0.01$  in  $0.001$  steps for Q2 and Q4 and from 0 to  $0.008$  in  $0.0005$  steps in the *lower panel*



contrasts with the results from Nagarajan et al. (2007), where a numerical computation of a dominant outer half of the boundary layer (close to the outer free stream) is performed. The main difference of the present experiments

with the experiments by Nolan et al. (2010) is that, in this experiment, there is an moving interface (water waves moving in the tank) instead of a fixed rigid wall. This difference results in the initiation of turbulence spots due to

several possible mechanisms, such as flow separation near the wave crest, as reported in detail in the analysis of Shaikh and Siddiqui (2011a).

## 7 Conclusion

This study detailed the structure of turbulence in the air-side boundary layer with a mean flow already analysed in a previous study.

- A comparison with the air flow over a plane smooth rigid wall showed a higher Reynolds stress with streamwise fluctuations largely dominant with respect to the vertical fluctuations. A rapid decline in turbulence was recorded in the domain where water was periodically present. A layer of constant shear Reynolds stress allowed a friction velocity with an excess value of approximately 20 %, more or less twice the excess value computed for the plane smooth rigid wall.
- The contribution of the wave-induced Reynolds stress was detected through filtering the spectrum of velocity fluctuations using a cut-off frequency equal to the peak of the spectrum of the free surface level. At least 50 % of the boundary layer structure was strongly influenced by wave-induced Reynolds stresses, even though  $H_{\text{rms}}$  is a better scale for the vertical distribution of these stresses. Wave-induced Reynolds stresses became negligible for  $z > 5 H_{\text{rms}}$ .
- The distribution of the intermittency factor in the boundary layer over water waves was similar to that in a boundary layer over a rigid plane wall, with several differences near the interface. Here, the presence/absence of water damps out the turbulence.
- The quadrant analyses revealed that ejection and sweep events were dominant and more concentrated. The joint p.d.f. of the fluctuating velocities,  $U'$  and  $V'$ , exhibited circular isolines in the upper region of the boundary layer ( $z/\delta > 0.7$ ), which became elliptic in the lower region, near the water interface. At small fetches, the large-amplitude negative streamwise perturbations were preferentially lifted. For larger fetches, ejections and sweeps were concentrated near the water interface. The intensity of momentum transfer from the wind stream to the gravity waves is much larger for the short growing wave characteristics of the present tests than for mature waves.
- Turbulence energy production peaked at  $z/\delta = 0.2$  and had a distribution similar to that observed for a self-preserving boundary layer with a strong adverse gradient pressure. The quadrant analysis contribution to the energy production revealed that ejections still dominated the balance and that the production was

spatially modulated in the wind direction with a couple of cells and with a minimum in the area of the free surface wave height reduction.

**Acknowledgments** The experimental data presented herein were obtained during the author's sabbatical spent at CEAMA, Grupo de Dinámica de Flujos Ambientales, University of Granada, Spain, kindly hosted by Miguel A. Losada. Financial support from CEAMA is gratefully acknowledged. Special thanks to Luca Chiapponi, Simona Bramato and Christian Mans who provided great help with the experiments.

## References

- Alfredsson RJ, Johansson AV (1984) On the detection of turbulence-generating events. *J Fluid Mech* 139(1):325–345
- Anisimova YP, Makova VI, Nikitina YA, Speranskaya AA (1982) Momentum flux spectrum above a developing wind wave. *Atmos Oceanic Phys* 18:435–439
- Antonia RA, Chambers AJ (1980) Wind wave induced disturbances in the marine surface layer. *J Phys Oceanogr* 10:611–622
- Brocchini M (2002) Free surface boundary conditions at a bubbly/weakly-splashing air-water interface. *Phys Fluids* 14(6):1834–1840
- Brocchini M, Peregrine DH (2001) The dynamics of strong turbulence at free surfaces. Part 2. Free-surface boundary conditions. *J Fluid Mech* 449:255–290
- Chang PC, Plate EJ, Hidy GM (1971) Turbulent air flow over the dominant component of wind-generated water waves. *J Fluid Mech* 47:183–208
- Chiapponi L, Longo S, Bramato S, Mans C, Losada A M (2011) Free-surface turbulence, Wind generated waves: laboratory data. Technical report on experimental activity in Granada, University of Parma (Italy), CEAMA (Granada, Spain)
- Donelan MA, Babanin AV, Young IR, Banner ML (2006) Wave-follower field measurements of the wind-input spectral function. Part II: parameterization of the wind input. *J Phys Oceanogr* 36:1672–1689
- Foster RC, Vianey F, Drobinski P, Carlotti P (2006) Near-surface coherent structures and the vertical momentum flux in a large-eddy simulation of the neutrally-stratified boundary layer. *Boundary Layer Meteorol* 120:229–255
- Hsu C-T, Hsu E-Y (1983) On the structure of turbulent flow over a progressive water wave: theory and experiment in a transformed, wave-following coordinate system. Part 2. *J Fluid Mech* 131:123–153
- Hsu C-T, Hsu E-Y, Street RL (1981) On the structure of turbulent flow over a progressive water wave: theory and experiment in a transformed, wave-following coordinate system. *J Fluid Mech* 105:87–117
- Hunt JCR, Stretch DD, Belcher SE (2011) Viscous coupling of shear-free turbulence across nearly flat fluid interfaces. *J Fluid Mech* 671(iii):96–120
- Janssen PAEM (1999) On the effect of ocean waves on the kinetic energy balance and consequences for the inertial dissipation technique. *J Phys Oceanogr* 29:530–534
- Kato H, Sano K (1971) An experimental study of the turbulent structure of wind over water waves. *Rep Port Harb Res Inst* 10:3–42
- Klebanoff PS (1955) Characteristics of turbulence in a boundary layer with zero pressure gradient. NACA Report 1247
- Krostad PÅ, Antonia RA (1999) Surface roughness effects in turbulent boundary layers. *Exp Fluids* 27:450–460

- Lam K, Banerjee S (1992) On the condition of streak formation in a bounded turbulent flow. *Phys Fluids A Fluid Dyn* 4(2):306–320
- Letchford CW, Zachry BC (2009) On wind, waves, and surface drag. Presented at the 5th European and African conference on wind engineering, Florence, Italy
- Longo S (2010) Experiments on turbulence beneath a free surface in a stationary field generated by a Crump weir: free surface characteristics and the relevant scales. *Exp Fluids* 49:1325–1338
- Longo S (2011) Experiments on turbulence beneath a free surface in a stationary field generated by a Crump weir: turbulence structure and correlation with the free surface. *Exp Fluids* 50:201–215
- Longo S (2012) Wind-generated water waves in a wind tunnel: free surface statistics wind friction and mean air flow properties. *Coastal Eng* 61:27–41
- Longo S, Liang D, Chiapponi L, Aguilera Jiménez L (2012) Turbulent flow structure in experimental laboratory wind-generated gravity waves. Accepted in *Coastal Engineering*. doi: [10.1016/j.coastaleng.2012.02.006](https://doi.org/10.1016/j.coastaleng.2012.02.006)
- Miles JW (1957) On the generation of surface waves by shear flows. *J Fluid Mech* 3:185–204
- Miles JW (1959) On the generation of surface waves by shear flows. *J Fluid Mech* 6:568–582
- Nagarajan S, Lele SK, Ferziger JH (2007) Leading-edge effects in bypass transition. *J Fluid Mech* 572:471–504
- Nolan KP, Walsh EJ, McEligot DM (2010) Quadrant analysis of a transitional boundary layer subject to free-stream turbulence. *J Fluid Mech* 658:310–335
- Rashidi M, Banerjee S (1990) The effect of boundary conditions and shear rate on streak formation and breakdown in turbulent channel flows. *Phys Fluids A* 2(10):1827–1838
- Schlichting H, Gersten K (2000) *Boundary layer theory*. Springer, Berlin
- Shaikh N, Siddiqui K (2011a) Near-surface flow structure over wind-generated water waves, part I: wave-induced flow characteristics. *Ocean Dyn* 61:127–141
- Shaikh N, Siddiqui K (2011b) Near-surface flow structure over wind-generated water waves, part II: characteristics of separated and non-separated flows. *Ocean Dyn* 61:143–154
- Sjöblom A, Smedman AS (2002) The turbulent kinetic energy budget in the marine atmospheric surface layer. *J Geophys Res* 107(C10):3142
- Sjöblom A, Smedman AS (2003) Vertical structure in the marine atmospheric boundary layer and its implication for the inertial dissipation method. *Boundary-Layer Meteorol* 109:1–25
- Stewart RH (1970) Laboratory studies of the velocity field over deep-water waves. *J Fluid Mech* 42:733–754
- Sullivan PP, McWilliams JC, Moeng C-H (2000) Simulation of turbulent flow over idealized water waves. *J Fluid Mech* 404:47–85
- Sullivan PP, Edson JB, Hristov T, McWilliams JC (2008) Large-Eddy simulations and observations of atmospheric marine boundary layers above nonequilibrium surface waves. *J Atmos Sci* 65:1225–1245
- Townsend AA (1948) Local isotropy in the turbulent wake of a cylinder. *Aust J Sci Res Ser A Phys Sci* 1:161–174
- Townsend AA (1976) *The structure of turbulent shear flow*. Cambridge University Press, Cambridge
- Yelland M, Taylor PK (1996) Wind stress measurements from the open ocean. *J Phys Oceanogr* 26(4):541–558